

**Non-Local Damage Modeling of Rocks under the conditions of
High Pressure and High Temperature (HPHT)**

Submitted in partial fulfillment of the requirements for

the degree of

Doctor of Philosophy

in

Civil and Environmental Engineering

Mudasar Zahoor

B.Tech., Civil Engineering, National Institute of Technology, Srinagar, India
M.S., Civil and Environmental Engineering, Carnegie Mellon University

Carnegie Mellon University
Pittsburgh, PA

August 2011

Acknowledgements

I would like to take this opportunity to sincerely thank all my friends and family who supported me throughout the course of my PhD. A special word appreciation goes to my dearest friends, Saurabh Puri and Asli Akcamete, who were always a big help on technical and motivational grounds.

I would also like to thank my advisor Prof. Amit Acharya for providing me the opportunity to work on this project and helping me out with many issues that arose at various stages of my PhD. I also acknowledge The National Energy Technology Laboratories (NETL) for funding this project.

I am most thankful to my committee members; Prof. Jacobo Bielak (Civil and Environmental Engineering, CMU), Dr. Craig Maloney (Civil and Environmental Engineering, CMU) and Dr. Enrique Bazan-Zurita (DiGioia Gray & Associates) for their feedback and suggestions.

Last but not the least, I would also like to thank all of the Civil and Environmental Engineering departmental staff especially Ms. Maxine Leffard and Mr. Curtis Yeske who have always been kind and helpful.

Abstract

This work is an attempt to develop a physically realistic model to understand the behavior and failure of rocks, especially under the extreme conditions of High Pressure and High Temperature (HPHT). A platform is laid in the preliminary work where 1D pure and ductile damage models are developed respectively. These models are based on an elasto-plastic model with an additional governing equation incorporated to facilitate the inclusion of damage. This additional governing equation is called the damage evolution equation. In the ductile damage model, it is assumed that the damage is driven and controlled by plasticity. The concepts developed in the preliminary work of 1D modeling are then taken into the study of 3D problems. The main problems studied are: the unconstrained uniaxial compression, the completely constrained uniaxial compression and the dynamic indentation problem. The dynamic indentation problem is the representation of an idealized rock drilling process. The results from the indentation problem are found to be in good qualitative agreement with the experimental results (Abd Al-Jalil, Y.Q 2006).

Contents

List of Notations	i
List of Figures	iv
List of Algorithms	x
1 Introduction	1
1.1 Overview	1
1.2 Literature Review	2
2 Preliminary Work	8
2.1 Dynamic Simple Shear Problem (1-D)	8
2.1.1 Introduction:	8
2.1.2 One-Dimensional Simple Shear – The Dynamic Elasto- Plastic Problem	9
2.1.3 Scheme for solving this problem	11

CONTENTS

ii

2.1.4	Material Behavior – Verification	12
2.1.5	Field Equations - Verification	16
2.1.6	Material Response	17
2.1.6.1	Rate-Independent Material	17
2.1.6.2	Rate-Dependent Material	20
2.1.7	Conclusion	23
2.2	Damage - Introduction and Formulation	23
2.2.1	Introduction	23
2.2.2	Damage and Free Energy	25
2.2.2.1	Choosing f and s	28
2.2.3	Dynamic 1-D Simple Shear Problem	30
2.2.3.1	Verifying the Damage Evolution equation: . . .	33
2.2.3.2	Results	33
2.3	Ductile/Plastic Damage (1-D)	37
2.3.1	Introduction	37
2.3.2	Dynamic 1-D Simple Shear Problem	39
2.3.2.1	Results	41
3	3D Ductile Damage	47
3.1	Introduction	47

<i>CONTENTS</i>	iv
4.2.1 Unconstrained Local	72
4.2.2 Unconstrained Non-Local	73
4.2.3 Unconstrained Local vs Non-Local	74
4.3 Completely Constrained Case	75
4.3.1 Completely Constrained Local	76
4.3.2 Completely Constrained Non-Local	77
4.3.3 Completely Constrained Local vs Non-Local	78
4.4 Unconstrained versus Completely Constrained Compression . .	79
5 The Dynamic Indentation Problem	82
5.1 Introduction	82
5.2 Indentor Modeling - Set up	83
5.3 Local Case	85
5.4 Non-Local Case	87
5.5 Temperature Effects	90
5.5.1 Exponential Law	93
5.5.2 Power Law	95
6 Conclusion	99
Bibliography	101

List of Notations

α	friction coefficient
α_ψ	dilatancy coefficient
β	diffusion coefficient
γ	equivalent plastic strain
\hat{n}	unit normal
κ	material constant
μ	shear modulus
ω	frequency
ψ	free energy
ρ	mass density
σ	stress
σ'	deviatoric stress
τ	flow stress
τ_{eq}	effective stress

τ_h	hydrostatic stress
τ_{y0}	initial flow stress
$\tau_{y\infty}$	residual flow stress
Θ	temperature
Θ_0	standard temperature at ground level
Δt	time step
Δt_d	time step from damage evolution equation
Δt_{wave}	time step from Courant condition
Δx	spatial spacing
$\underline{\underline{C}}$	modulus
\underline{f}	flux
ε	total strain
ε^p	plastic strain
φ	void-volume fraction
ϑ	positive material constant
ζ	saturation exponent
A	material constant
a	material parameter
B	positive constant
b	positive material constant

C_s	shear wave speed
D	energy dissipation rate
e_c	small positive dimensionless constant
f_d	initial displacement profile - D'Alembert solution
$G(\varphi)$	damage threshold
g_t	material parameter
h	height of the infinite plate
$H(\varepsilon^p)$	hardening function
h_p	linear hardening coefficient
j_{elem}	element number
k	wave number
L	length of the specimen
m	rate-sensitivity
N	time increment
p	pressure
s	source
T	run time
t	time
u	displacement
u_0	initial displacement

u_i	displacement in i direction, i=1,2,3
v	velocity
v_0	initial velocity
v_c	constant velocity at the top of the plate
w	damage driving variable
w_0	constant dependent on strain rate
w_{jelem}	damage driving variable corresponding to element jelem
X	position vector
x	coordinate
Y	damage energy release rate
Y_1	local damage threshold

List of Figures

2.1	Infinite plate of finite thickness	9
2.2	Results verifying material behavior (Elastic case) at time, T=0.001; (a) Linear variation of velocity with 'x', (b) Constant Stress with 'x', (c) Stress-Strain relationship for each node. <i>Units: (non-dimensionalized)</i>	14
2.3	Results verifying material behavior (Plastic case) at time, T=0.1; (a) Linear variation of velocity with 'x', (b) Constant Stress with 'x', (c) Stress-Strain relationship for each node. <i>Units: (non-dimensionalized)</i>	15
2.4	Initial Displacement (Gaussian). <i>Units: distance (m), displace- ment (m)</i>	17
2.5	Verification of D'Alembert solution at time, T=0.0001. <i>Units: distance (m), displacement (m)</i>	18

2.6	Initial Yield strength of the Rate-independent material. <i>Units: (non-dimensionalized)</i>	18
2.7	Material Response of a rate-independent material at Hardening and Softening, (a) Stress-Strain relation at Hardening (at $x=0.5$) at time, $T=0.05$, (b) Plastic Strain field plot at Hardening at time, $T=0.05$, (c) Stress-Strain relation at Softening (at $x=0.5$) at time, $T=0.1$, (d) Plastic Strain field plot at Softening at time, $T=0.1$. <i>Units: (non-dimensionalized)</i>	21
2.8	Material Response of a rate-insensitive material at Hardening and Softening; (a) Stress-Strain relation at Hardening (at $x=0.5$) at time, $T=0.05$, (b) Plastic Strain field plot at Hardening at time, $T=0.05$, (c) Stress-Strain relation at Softening (at $x=0.5$) at time, $T=0.125$, (d) Plastic Strain field plot at Softening at time, $T=0.125$. <i>Units: (non-dimensionalized)</i>	22
2.9	Material Response of a rate-sensitive material at Hardening and Softening; (a) Stress-Strain relation at Hardening (at $x=0.5$) at time, $T=0.05$, (b) Plastic Strain field plot at Hardening at time, $T=0.05$, (c) Stress-Strain relation at Softening (at $x=0.5$) at time, $T=0.5$, (d) Plastic Strain field plot at Softening at time, $T=0.5$. <i>Units: (non-dimensionalized)</i>	24
2.10	Verification result for the Damage Evolution equation. <i>Units: distance (m)</i>	34

2.11	Initial condition on void-volume fraction (in %). <i>Units: distance (m)</i>	34
2.12	Results for the Non-Local case after softening; (a) Field plot of Void-volume fraction, (b) Field plot of Strain, (c) Stress-Strain relation at the center. <i>Units: distance (m), stress (N/m²)</i> . . .	36
2.13	Initial condition on void-volume fraction (in %). <i>Units: distance (m)</i>	42
2.14	Results for the Local Case; (a) Field plot for void-volume fraction, (b) Field plot for strain, (c) Stress-Strain relation at the center. <i>Units: distance (m), stress (N/m²)</i>	43
2.15	Results for the Non-local case; (a) Field plot for void-volume fraction, (b) Field plot for strain, (c) Stress-Strain relation at the center. <i>Units: distance (m), stress (N/m²)</i>	45
2.16	Comparison between Local and Non-Local results; (a) Field plot for void-volume fraction, (b) Field plot for strain, (c) Stress-Strain curves. <i>Units: distance (m), stress (N/m²)</i> . . .	46
3.1	Three dimensional block used for verifying the governing equations. <i>Units: distance (m)</i>	54
3.2	Wave equation verification - Result for only one layer of nodes. <i>Units: distance (m), displacement (m)</i>	55

3.3	Diffusion equation verification - Result for only one layer of nodes. <i>Units: distance (m)</i>	56
3.4	Cube Specimen	58
3.5	Elasticity verification – Simple Shear. <i>Units: stress (N/m²)</i>	60
3.6	Plasticity verification – Simple-Shear (J2). <i>Units: stress (N/m²)</i>	61
3.7	Plasticity verification – Simple-Shear (Drucker-Prager). <i>Units: stress (N/m²)</i>	61
3.8	Material softening with damage (J2). <i>Units: stress (N/m²)</i>	62
3.9	Material softening with damage (Drucker-Prager). <i>Units: stress (N/m²)</i>	62
3.10	Elasticity verification – Tension. <i>Units: stress (N/m²)</i>	65
3.11	Plasticity verification (J2). <i>Units: stress (N/m²)</i>	66
3.12	Plasticity verification (Drucker-Prager). <i>Units: stress (N/m²)</i>	67
3.13	Material softening with damage (J2). <i>Units: stress (N/m²)</i>	68
3.14	Material softening with damage (Drucker-Prager). <i>Units: stress (N/m²)</i>	68
4.1	Uniaxial Compression Setup	70
4.2	Uniaxial Unconstrained Compression Setup	72
4.3	Av. Stress vs Av. Strain (LOCAL). <i>Units: stress (N/m²)</i>	74

4.4	Av. Stress vs Av. Strain (NON-LOCAL). <i>Units: stress (N/m^2)</i>	75
4.5	Av. Stress vs Av. Strain (LOCAL vs NON-LOCAL). <i>Units:</i> <i>stress (N/m^2)</i>	76
4.6	Uniaxial constrained compression setup	76
4.7	Av. Stress vs Av. Strain (LOCAL). <i>Units: stress (N/m^2)</i> . .	77
4.8	Av. Stress vs Av. Strain (NON-LOCAL). <i>Units: stress (N/m^2)</i>	78
4.9	Av. Stress vs Av. Strain (LOCAL vs NON-LOCAL). <i>Units:</i> <i>stress (N/m^2)</i>	79
4.10	Av. Constrained vs Unconstrained; (a) LOCAL, (b) NON- LOCAL. <i>Units: stress (N/m^2)</i>	81
5.1	Idealized Indentor showing rock body and damaged zone . . .	84
5.2	Typical Mesh Refinement	84
5.3	Displacement profile in the form of a Gaussian. <i>Units: distance</i> <i>(m), displacement (m)</i>	85
5.4	Average Stress versus Average Strain for two mesh sizes. <i>Units:</i> <i>stress (N/m^2)</i>	86
5.5	Field plots for void-volume fraction; (a) 150 elements, (b) 300 elements. <i>Units: distance (m)</i>	87
5.6	Average Stress versus Average Strain for different mesh sizes. <i>Units: stress (N/m^2)</i>	89

5.7	Field plots for void-volume fraction; (a) 150 elements, (b) 300 elements. <i>Units: distance (m)</i>	91
5.8	Field plots for stress; (a) 150 elements, (b) 300 elements. <i>Units: stress (N/m²), distance (m)</i>	92
5.9	Comparison: at two different temperatures. <i>Units: stress (N/m²)</i>	94
5.10	Comparison: at two different temperatures with higher value of 'a'. <i>Units: stress (N/m²)</i>	94
5.11	Comparison: different 'a' at same temperature. <i>Units: stress (N/m²)</i>	95
5.12	Comparison: at two different temperatures. <i>Units: stress (N/m²)</i>	96
5.13	Comparison: at two different temperatures with higher value of 'g'. <i>Units: stress (N/m²)</i>	97
5.14	Comparison: different 'g' at same temperature. <i>Units: stress (N/m²)</i>	98

List of Algorithms

2.1	One-dimensional Plastic Damage	40
3.1	Working mechanism for 2D/3D Non-local ductile damage . . .	52

Chapter 1

Introduction

1.1 Overview

The concept of pure damage or the nucleation and evolution of voids is the primary phenomenon responsible for rock failure. The study of damage of rocks, around which this research revolves, in particular under conditions of High Pressure and High Temperature (HPHT), is desired. The behavior of rocks under HPHT is very different than under the conditions of normal pressure and normal temperature. A rock, which is otherwise a brittle material, behaves more like a metal showing ductile behavior under the conditions of HPHT. Due to confinement, the fragments can stay together and flow like a continuum thus demonstrating ductile behavior. It must be noted that voids can play a role in metal behavior (Horstemeyer, M.F., Gokhale, A.M. 1999)

as well, however, most studies do not consider the effect of voids.

In dynamics, the case of interest for rock cutting, the typical softening in strength along with non-associated flow in the formation behavior results in the loss of hyperbolicity, i.e. wave speeds become imaginary, resulting in localized stationary waves and the problem becomes ill posed. The conventional models and theories of material behavior have no intrinsic material length scale, thereby, predicting deformation bands of zero thickness, which is physically incorrect. The main purpose of this research is to explore the development of a 3D non-local macroscopic model of combined brittle-ductile damage for the realistic modeling of the behavior of rocks under HPHT conditions.

1.2 Literature Review

The state-of-the-art in continuum damage modeling and analysis of quasi-brittle material was assessed, within the context of modeling rock failure behavior under normal and high temperature and high-pressure conditions.

The primary issue requiring resolution in our failure modeling effort is that local continuum constitutive models for physically realistic, rate-independent, strain softening behavior of quasi-brittle materials, i.e. materials for which the fracture process zone size is not negligible in comparison to the characteristic structural length scale, do not render the (initial) boundary value problems well-posed. The inclusion of material rate dependence along with

inertial effects provide stability against perturbations and introduces a size effect, but this is not found to be sufficient in predicting a finite width of deformation banding (e.g. shear bands) characteristic of intense deformation and failure. Thermal conductivity can provide such a length scale for deformation banding, but its relevance in the deformation of quasi-brittle materials may be questioned, especially in slow motions. Instead, for such materials the damage process is believed to be non-local, and the length scales arising from the accurate modeling. Non-Local Damage Modeling of Rocks under the conditions of HPHT is expected to result in the realistic modeling of strain-softening intense deformations to failure.

Rudnicki and Rice (1975) is a classic for introducing the concept of bifurcation as a condition for localization into mainstream solid mechanics, following the works of Hadamard, Thomas, and Hill. The general theory is applied to shear banding in pressure sensitive dilatant materials and the inception of rupture is understood as a constitutive instability.

Pijaudier-Cabot and Bazant (1988) provide the first nonlocal damage model where the strains are local but the damage evolution is nonlocal. Historically, this is an important paper as it showed that nonlocal damage mechanics could be formulated and implemented in a robust and relatively simple manner.

The papers by Shawki (1994 a,b) analyze in detail the onset of shear localization in thermo- viscoplastic materials. The mathematical analysis clearly shows that a well-posed setting for understanding localization in a local

constitutive setting requires both inertia and rate-sensitivity. In addition, thermal conductivity sets a material length scale for hear bandwidth prediction. The conclusions of these papers will be useful for the present proposal when accounting for rate dependence and inertia.

Peerlings, De Borst, Brekelmans and DeVree (1996) discuss Laplacian enhanced nonlocal damage modeling for quasi-brittle materials from the numerical standpoint. This work is a subset of the paper discussed above.

The paper by Acharya, Cherukuri and Govindarajan (1999) discusses gradient regularization of rate-independent softening plasticity through gradient enhancement of work-hardening. The stabilizing effect of gradients as well as mesh-independence of results in dynamic deformation is demonstrated. While this method is adequate in postponing overall softening as is appropriate for metal softening due to thermal effects, it is unlikely to be suitable for the response of quasibrittle materials.

Bazant and Zi (2003) apply the microplane idea to the modeling of porous isotropic rock, in particular, those found in between joints. Of special note is the accounting of the effects of pore collapse on volume change in triaxial loading and reduction of frictional strength, recovery of frictional strength during shearing, and shear enhanced compaction in triaxial test, manifested by a deviation from the hydrostatic stress-strain curve. The paper also provides a stress update algorithm for implementation in explicit finite element codes, as well as details of data fitting.

The paper by Regenauer-Lieb and Yuen (2003) describes localization processes in igneous rocks. Modeling techniques involving rate dependence, inertia, heat conduction and the presence of water are discussed and modeled by the finite-element method.

Bazant (2004) presents an interesting, insightful theory of scaling of quasibrittle materials predominantly related to the understanding of the size effect.

The paper by Bazant and Di Luzio (2004) describes a nonlocal microplane model with strain softening yield limits that can be useful as a material model for rock in our project. In particular, a very desirable property of this model is the ability to model complete loss of load transfer capability, with deformation not localizing in a band of zero thickness, verified through numerical computations. The ‘Microplane model’ is a material model motivated by crystal plasticity. In the model, macroscopic stress is assumed to be an average of stress response over differently oriented planes whose deformation is assumed to be the projection of the macroscopic strain on the planes through a suitable, invariant definition (much like the resolved shear stress on slip planes in crystal plasticity). This allows for realistic predictions of anisotropy of failure arising from accounting of various failure mechanisms like tensile microcracking, slip, friction, lateral confinement, splitting and lateral spreading due to compression, and the collapse and closing of failures. The computational and calibration burden of these models, however, are somewhat heavy.

The paper by Carol, Jirasek, and Bazant (2004) lays out the local microplane framework at finite strains in a thermodynamic setting and applies it to hyper-elasticity as a test case. These ideas coupled with those of Bazant and Di Luzio is a viable approach to the modeling for our project.

Hoek, Carranza-Torres, and Corkum (2004) provide the latest version (to our knowledge) of the Hoek-Brown failure criterion by clarifying certain uncertainties and inaccuracies of earlier versions of the same model. In combination with some nonlocal modeling ideas, this popular rock mechanics model could be a viable alternative for our failure modeling.

Abd Al-Jalil (2006) presents a critical review of research on the indentation of rock and rock cutting using disc cutters, such as those installed on tunnel boring machines. Observations from field tests, laboratory indentation tests, and linear cutter tests are presented. The mechanics of indentation of brittle rock types and chip formation is explained. A summary of the mechanics of indentation, fracture initiation, and chip formation is also presented.

The paper by Abendroth and Kuna (2006) presents a method for the identification of deformation, damage and fracture properties of ductile materials. The small punch test is used to obtain the material response under loading.

Aydin, Borja, and Eichhubl (2006) classify failure modes in granular rocks into two categories of strong discontinuities (crack-like failure) and weak discontinuities (tabular structures resulting from strain localization). In both cases, the modes can be redominated by shear and/or volumetric deformation

with a continuous spectrum. The mathematical analysis of the paper focuses on weak discontinuities (strain localization) using classical bifurcation theory first introduced in the paper by Rudnicki and Rice (1975) in the context of geomaterials. The authors formulate a family of three invariant plasticity models with a compression cap that captures the initiation of failure for the entire spectrum of observed geological strain localization failure modes.

The paper by Mediavilla, Peerlings, and Geers (2006) develops damage Laplacian based gradient damage model for ductile failure, accounting for stress triaxiality. The Laplacian model of nonlocality is the most convenient for numerical implementation, and is shown to work robustly down to failure, i.e. loss of load carrying capacity. Hence, finding a physical justification for the Laplacian regularization of softening due to damage would be very desirable from the modeling point of view. With regard to failure modeling for this proposal, this regularization coupled with any of the above mentioned local models of rock failure would be appropriate.

Acharya (2009) suggests a technique for setting up generalized continuum theories based on a balance law and nonlocal thermodynamics. The methodology does not require the introduction of gradients of the internal variable in the free energy, while allowing for its possibility. As an example, elements of a generalized damage model with porosity as the internal variable are developed.

Chapter 2

Preliminary Work

2.1 Dynamic Simple Shear Problem (1-D)

2.1.1 Introduction:

To start with, we considered a dynamic one-dimensional simple shear problem (Acharya, et al 1999) to understand the effect of external forces and the material response with the classical theory only (no non-local effects were considered). The responses of rate-independent and rate-sensitive materials were studied respectively.

2.1.2 One-Dimensional Simple Shear – The Dynamic Elasto-Plastic Problem

Consider a one-dimensional simple shearing of an infinite plate of finite width as shown in Figure 2.1. The top of the plate is subjected to a constant velocity v_c while the bottom is kept fixed. Practically, the case of simple shear corresponds to the situation where a tube of finite thickness is subjected to a torque.

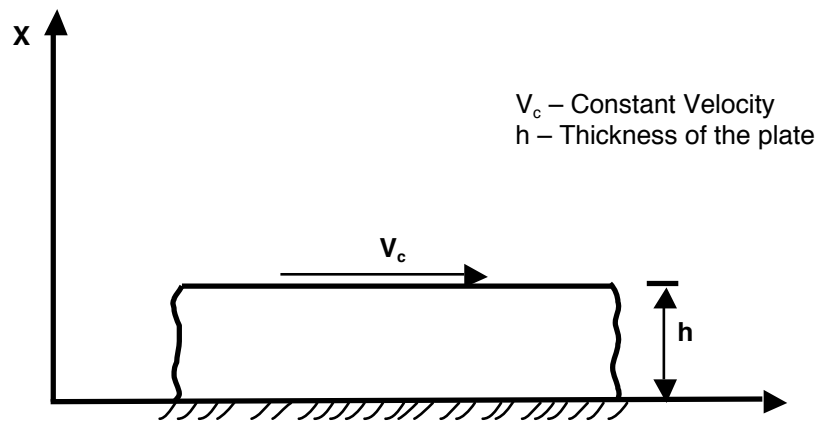


Figure 2.1 – Infinite plate of finite thickness

The governing equations for the balance of linear momentum and the elastic stress-strain relation are of the form:

$$\rho \dot{v} = \sigma_{,x} \quad (2.1)$$

and

$$\dot{\sigma} = \mu (\dot{\varepsilon} - \dot{\varepsilon}^p) \quad (2.2)$$

The yield condition, flow rule and hardening law are given by:

$$\begin{aligned} y(\sigma, \tau) &= |\sigma| - \tau \leq 0, \tau \geq 0 \\ \dot{\varepsilon}^p &= \dot{\gamma} \text{sign}(\sigma), \dot{\gamma} \geq 0 \\ \dot{\tau} &= H(\gamma) \dot{\gamma} \end{aligned} \quad (2.3)$$

where, ρ is the mass density, v is the velocity, $\sigma_{,x}$ is the stress gradient, σ is the shearing stress parallel to the shearing direction, μ is the shear modulus, ε is the total strain, ε^p is the plastic strain, τ is the initial yield stress, $y(\sigma, \tau)$ is the yield function and $H(\gamma)$ is the hardening function (Tangent Modulus).

For the problem under consideration, $\sigma \geq 0$, which means that the material is loaded in only one direction and implies that $\gamma = \varepsilon^p$. Therefore, the quantities γ and ε^p can be used interchangeably. In particular, we can rewrite the hardening function as $H(\varepsilon^p)$. The hardening function in the present case is assumed to be of the form:

$$H(\varepsilon^p) = -2.7(2\varepsilon^p - 0.7) \quad (2.4)$$

The hardening function is responsible for introducing plasticity in the model. It is the tangent modulus given by flow stress – plastic strain curve. When the hardening function becomes zero, it indicates the onset of softening.

2.1.3 Scheme for solving this problem

The dynamic elasto-plastic problem is solved numerically using the Finite Difference technique. The space-time domain is discretized so as to have equispaced points with “ Δx ” and “ Δt ” as the spatial spacing and time steps respectively. The time step, Δt is calculated from the Courant condition in order to maintain numerical stability as follows:

$$C_s \Delta t \leq 2\Delta x, \text{ where, } C_s = \sqrt{\frac{\mu}{\rho}} \quad (2.5)$$

Even during plastic behavior the time step determined above is used, as this time step is always on the conservative side.

Once the above model was developed, its verification with respect to material behavior and field equations was done prior to using the model for various material studies. The material behavior was verified by field plots of velocity and stress and by the Stress-Strain relationship for the elastic and the plastic cases respectively. They were compared to their analytical counterparts. The governing equations were verified by comparing the numerical solution with the standard D’Alembert solution.

2.1.4 Material Behavior – Verification

The material behavior was verified by field plots of velocity and stress and by the Stress-Strain relationship for the elastic and the plastic cases respectively. We considered a homogeneous and isotropic material for this verification.

Initial Conditions:

- On velocity: $v(x, 0) = x$, which is a linear velocity profile
- On stress: $\sigma(x, 0) = 0$, i.e. the material is stress free at time $t = 0$

Boundary Conditions:

- On velocity: $v(0, t) = 0$, which implies a fixed base and $v(h, t) = v_0$, i.e. a constant velocity at the top of the plate

Note that we chose $h = 1$ and $v_0 = 1$.

The velocity profile $v(x, t) = x$ is a solution to our governing equation that satisfies the above mentioned initial and boundary conditions. Now from $v(x, t) = x$, we have:

$$\dot{v} = \frac{\partial v}{\partial t} = 0 \quad (2.6)$$

And from the governing equation, $\rho\dot{v} = \sigma_{,x}$, we get:

$$\sigma_{,x} = \frac{\partial \sigma}{\partial x} = 0 \quad (2.7)$$

which implies a uniform stress distribution throughout the body. Moreover, if the loading history is such that the material is plastically loading at all times, then (2.3) implies $\sigma(x, t) = \tau(t)$, i.e. σ follows the input flow stress – plastic strain curve.

These results can now be compared with the ones that were achieved numerically. The yield strength of the material was assumed to be 0.75 (non-dimensionalized). The results from the numerical simulation are shown graphically in Figures 2.2 and 2.3. Figure 2.2 shows results for the elastic case at time, $T=0.001$ when we are still within the yield value. The results are in perfect harmony with the expected analytical ones, which verifies the material behavior for the elastic case. In particular, the slope of the stress-strain curve is exactly equal to the chosen shear modulus value.

On the other hand, Figure 2.3 shows results for the plastic case at time, $T=0.1$, after initial yield has taken place. Here also we have a linear velocity profile and a uniform stress state throughout the body. In particular, the numerical and the analytical stress versus plastic strain curves are a perfect match of each other verifying the material behavior for the plastic case. The analytical curve is arrived at by integrating the hardening function (equation (2.4)) and getting the relation between flow stress, τ and plastic strain.

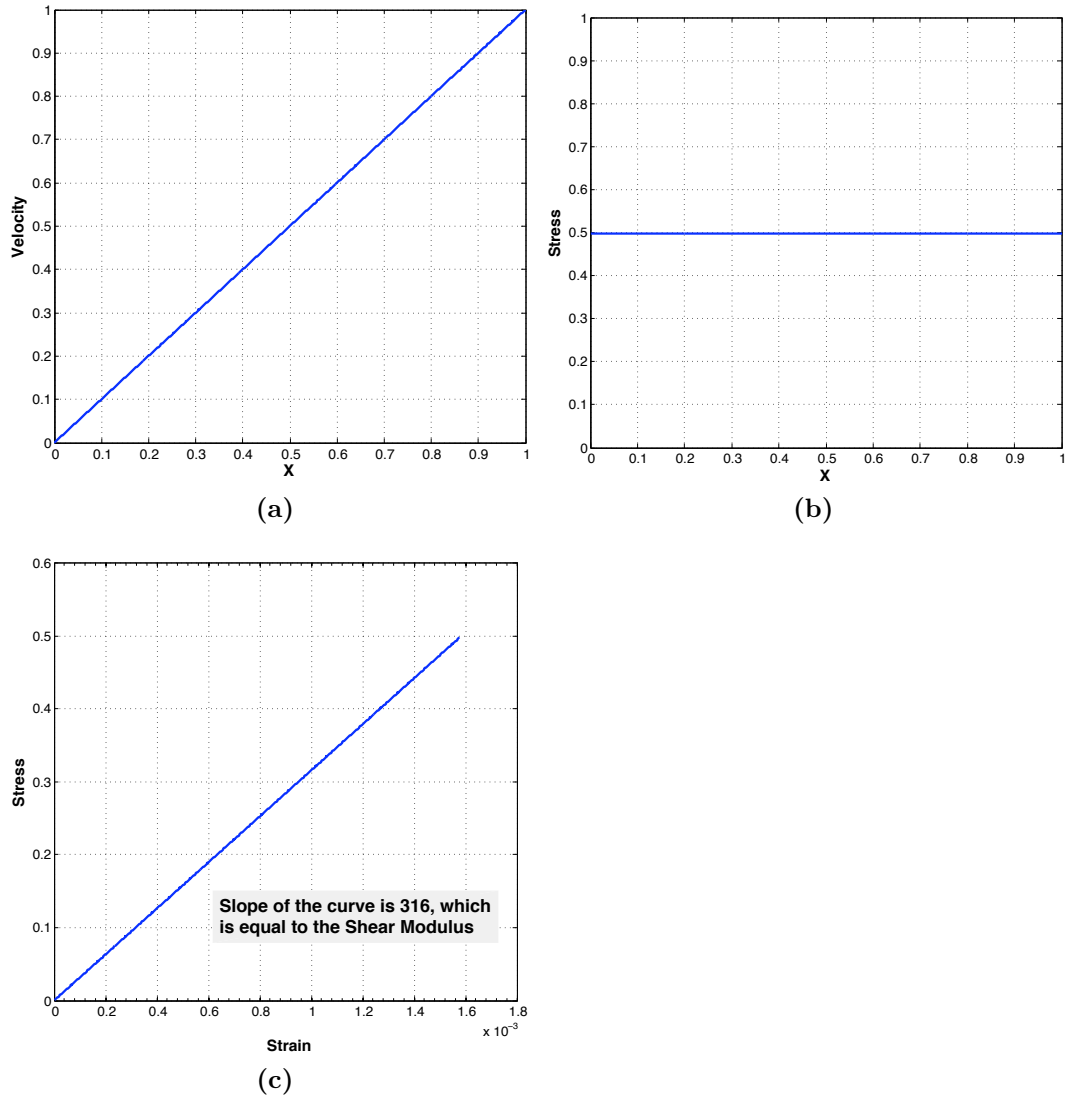


Figure 2.2 – Results verifying material behavior (Elastic case) at time, $T=0.001$; (a) Linear variation of velocity with 'x', (b) Constant Stress with 'x', (c) Stress-Strain relationship for each node. *Units: (non-dimensionalized)*

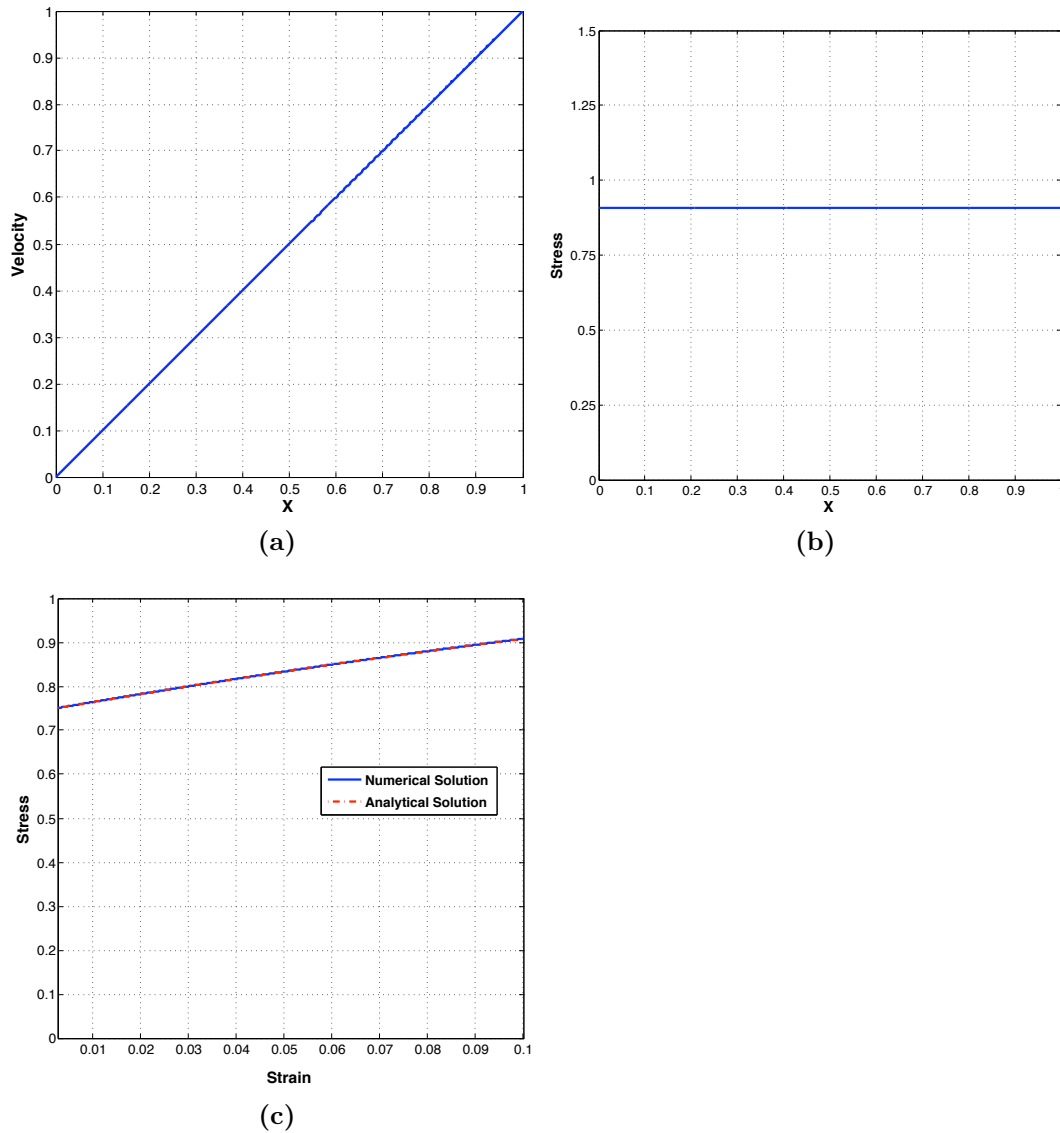


Figure 2.3 – Results verifying material behavior (Plastic case) at time, $T=0.1$; (a) Linear variation of velocity with 'x', (b) Constant Stress with 'x', (c) Stress-Strain relationship for each node. *Units: (non-dimensionalized)*

2.1.5 Field Equations - Verification

The numerical solution of the governing equations was verified by comparing it with the standard D'Alembert solution. The balance of linear momentum equation generates a wave motion, which for a linear elastic material must satisfy the classical D'Alembert solution. We considered an initial displacement in the form of a smooth Gaussian as shown in Figure 2.4 with prescribed initial velocity equal to zero.

The classical D'Alembert solution for the given problem is of the form:

$$u(x, t) = \frac{1}{2} [f_d(x - ct) + f_d(x + ct)]$$

where f_d is the initial displacement profile. This describes two waves of same amplitude traveling in opposite directions at exactly the same velocities emerging from a single disturbance of double their amplitude.

Figure 2.5 shows the result for the displacement that was achieved numerically at time, $T=0.0001$. It is clear that the result is a perfect representation of the above-mentioned D'Alembert solution. Further, comparing the standard value of velocity of propagation for a particular type of material with the value calculated from the graph provided an additional check. For example, for steel, the shear wave speed is determined from the relation:

$$C_s = \sqrt{\frac{\mu}{\rho}} = 3172 \text{ m/s}$$

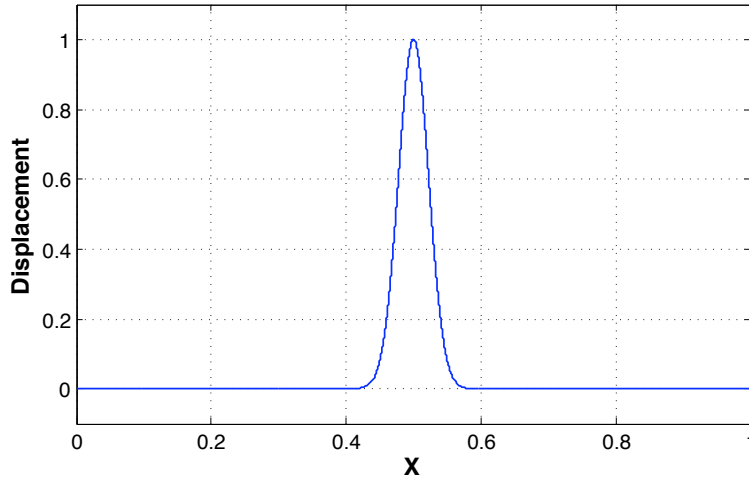


Figure 2.4 – Initial Displacement (Gaussian). *Units: distance (m), displacement (m)*

where, μ ($79e9 Pa$) is the elastic shear modulus of steel and ρ ($3750 kg/m^3$) is the mass density of steel.

The velocity of propagation calculated using Figure 2.5 was $3172 m/s$, which is exactly equal to the standard value.

2.1.6 Material Response

2.1.6.1 Rate-Independent Material

After the verification of material behavior and field equations, we moved to the next step and studied the response of a rate-independent material subjected to dynamic loading. The material was assumed to be non-homogeneous with the initial yield strength profile as shown in Figure 2.6. Please note that the

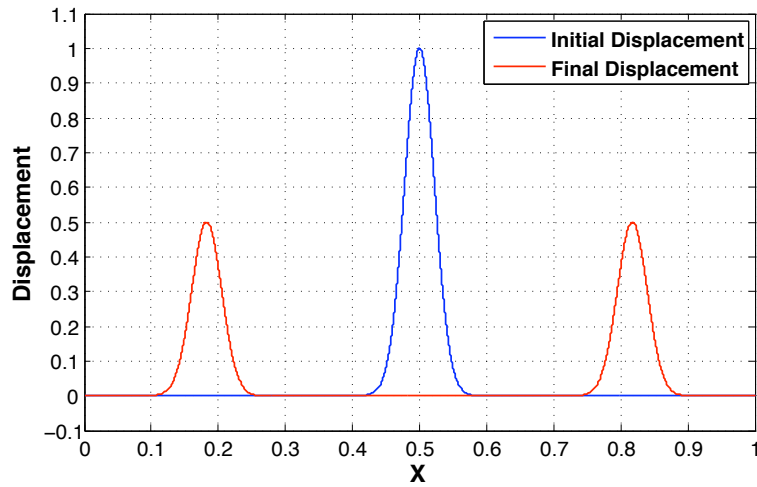


Figure 2.5 – Verification of D’Alembert solution at time, $T=0.0001$. *Units: distance (m), displacement (m)*

problem is non-dimensionalized.

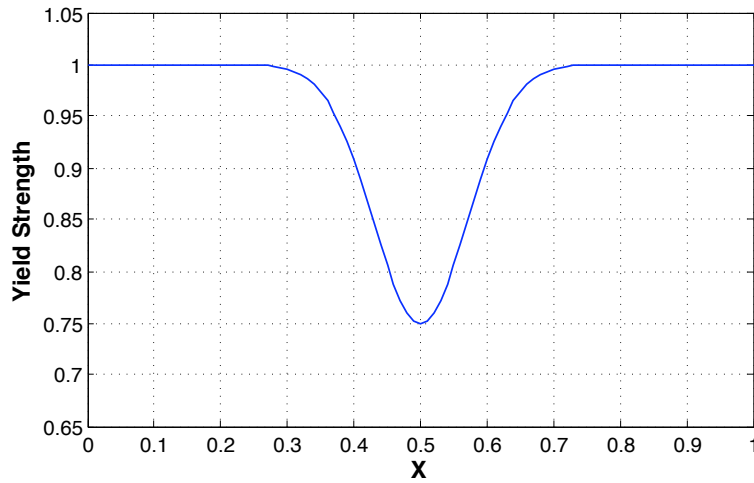


Figure 2.6 – Initial Yield strength of the Rate-independent material. *Units: (non-dimensionalized)*

The calculations were carried out to observe the effect of mesh size on material response at hardening and later softening stages respectively. Figure 2.7 shows

the results for a rate-independent material for three mesh refinements; 100, 1000 and 10000 elements respectively.

During the hardening phase, the governing equations are hyperbolic and we have a well defined solution (well-posed). In other words there is mesh independence as is clear from Figures 2.7(a) and 2.7(b). However, at softening there is loss of hyperbolicity, i.e. wave speeds become imaginary and the problem becomes ill posed. In other words there is no convergence at softening. In addition, the classical theory does not have any intrinsic material length scale and consequently the theory predicts deformation bands of zero thickness, which is why we see the mesh dependence as shown in Figure 2.7(d). Mathematically, the explanation of the loss of hyperbolicity is shown below:

The balance of linear momentum equation takes the form:

$$\frac{\partial^2 u}{\partial t^2} = \frac{1}{\rho} \left(\frac{H}{1 + \frac{H}{\mu}} \right) \frac{\partial^2 u}{\partial x^2}$$

Here, u is displacement, H is hardening function and μ is elastic shear modulus.

We assume one of the solutions to the above equation of the form, $e^{i(kx+\omega t)}$.

This implies:

$$\omega^2 = \frac{1}{\rho} \left(\frac{H}{1 + \frac{H}{\mu}} \right) k^2$$

Or

$$\omega = \pm k \sqrt{\frac{1}{\rho} \left(\frac{H}{1 + \frac{H}{\mu}} \right)}$$

When H is negative, the square root term becomes imaginary. Therefore, no matter how small t is, there will be a wave number k large enough that blows up the solution.

2.1.6.2 Rate-Dependent Material

In the previous case there was no material dictated rate-dependent dissipation. We now present our results for materials with rate-dependent dissipation. We considered two cases with same strain rate equal to $10^2 s^{-1}$;

Case I: Material with low rate-sensitivity (rate-insensitive material), e.g. Steel with rate- sensitivity, $m=0.019$

Case II: Material with high rate-sensitivity, $m=0.3$. This is a fictitious material used for the purpose of illustration.

It is important to mention here that the material properties, initial and boundary conditions were kept the same as for the rate-independent case.

Figure 2.8 shows results for a rate-insensitive material during hardening and at softening respectively for the three mesh refinements; 100, 1000 and 10000 elements respectively. During the hardening phase (Figures 2.8(a) and 2.8(b)), we notice that there is mesh independence and of course convergence. But during the softening stage, we see that the deformation zone gets thinner with decreasing mesh size, which clearly indicates mesh dependence at softening which is a similar response of a rate-independent material. Therefore, we confirm rate-insensitivity for this material, owing to its low value of ' m '.

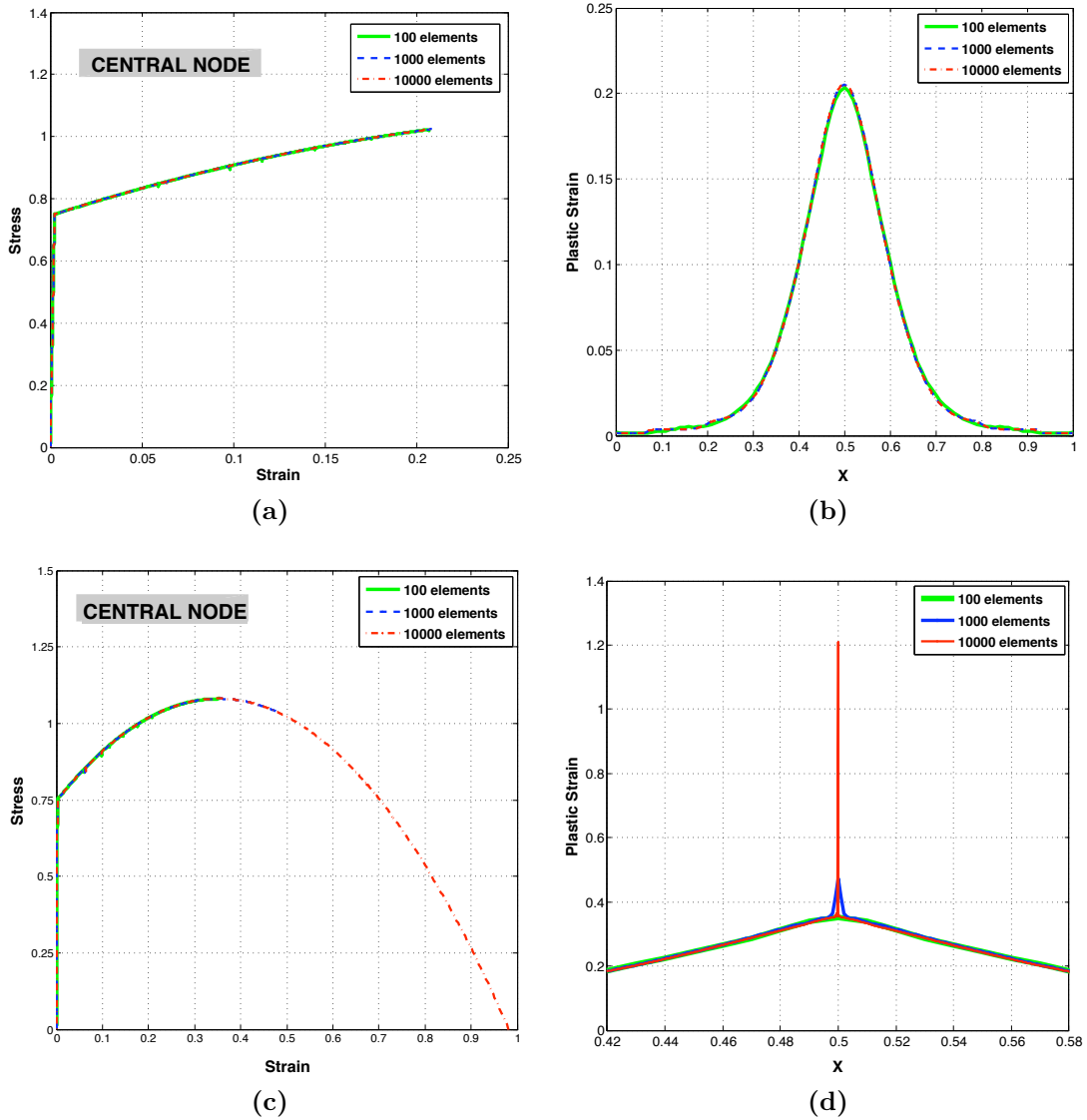


Figure 2.7 – Material Response of a rate-independent material at Hardening and Softening, (a) Stress-Strain relation at Hardening (at $x=0.5$) at time, $T=0.05$, (b) Plastic Strain field plot at Hardening at time, $T=0.05$, (c) Stress-Strain relation at Softening (at $x=0.5$) at time, $T=0.1$, (d) Plastic Strain field plot at Softening at time, $T=0.1$. *Units: (non-dimensionalized)*

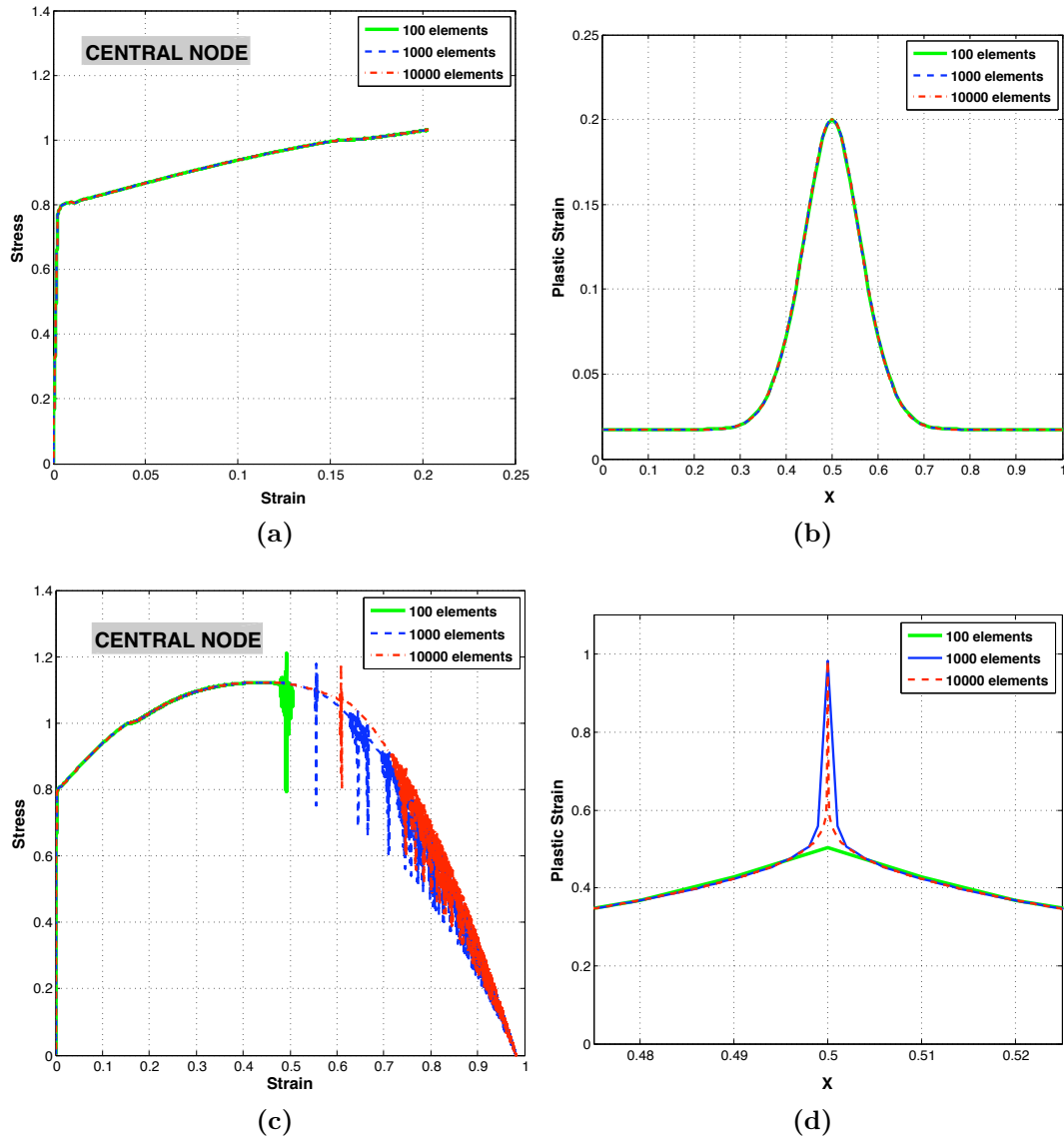


Figure 2.8 – Material Response of a rate-insensitive material at Hardening and Softening; (a) Stress-Strain relation at Hardening (at $x=0.5$) at time, $T=0.05$, (b) Plastic Strain field plot at Hardening at time, $T=0.05$, (c) Stress-Strain relation at Softening (at $x=0.5$) at time, $T=0.125$, (d) Plastic Strain field plot at Softening at time, $T=0.125$. *Units: (non-dimensionalized)*

Figure 2.9 shows results for a rate-sensitive material during hardening and at softening respectively for the three mesh refinements; 100, 1000 and 10000 elements respectively.

The rate-sensitive material behaves differently at softening compared to the rate-independent and the rate-insensitive material. We see mesh independence at softening with the results converging for the three mesh sizes. The high value of material rate-sensitivity adds to the stability, thereby, showing convergence.

2.1.7 Conclusion

The results presented are as expected from theory and in thorough conformity with the classical plasticity theory. However, it would be interesting to see the behavior of this model when non- local effects are applied.

2.2 Damage - Introduction and Formulation

2.2.1 Introduction

In the last section, the results from conventional Elasto-Plasticity theory applied to the Dynamic 1-D Simple Shear problem were presented. Mesh size dependence for rate- independent and rate-insensitive materials and mesh size independence for rate-sensitive materials respectively, were shown at softening.

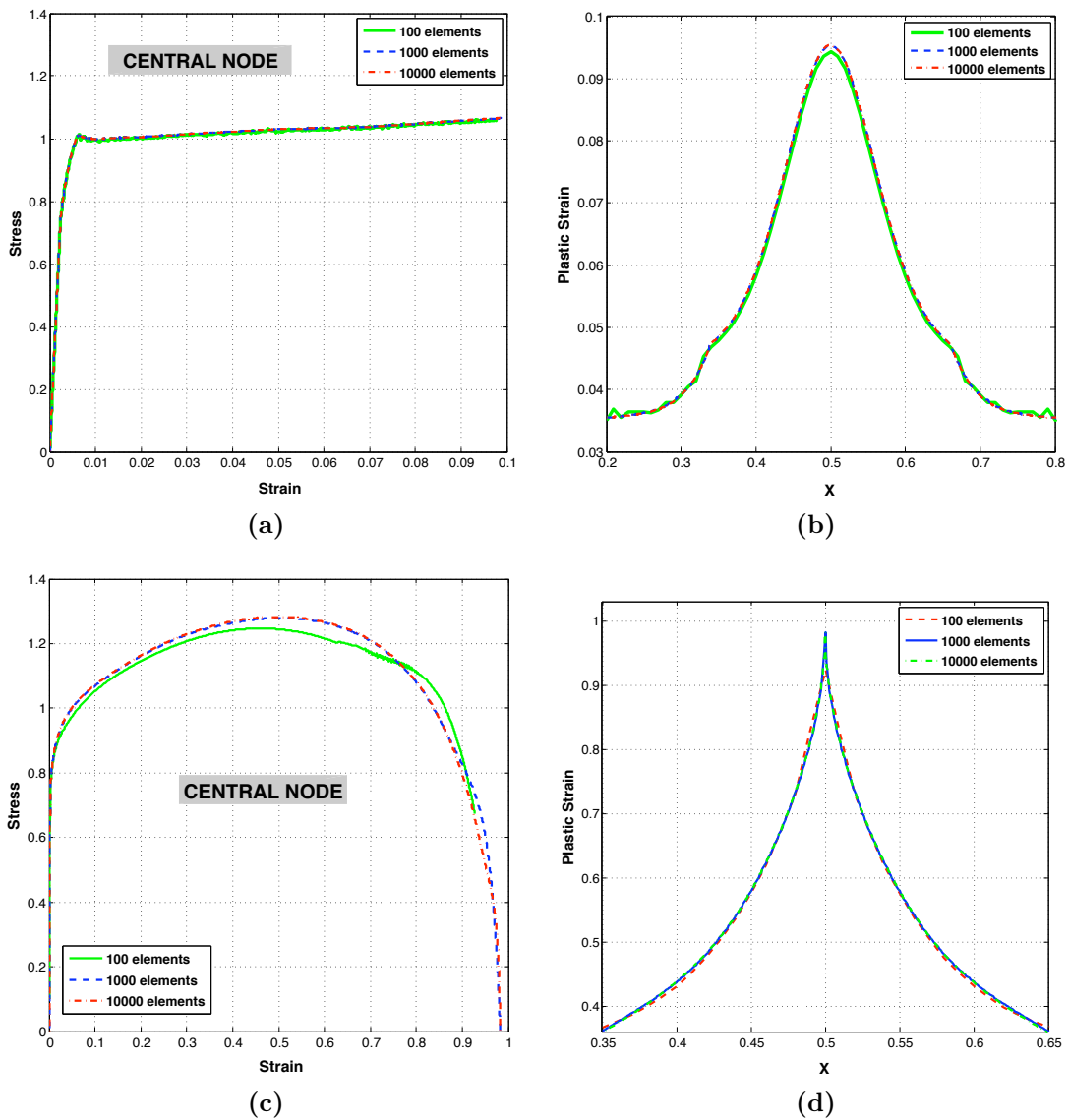


Figure 2.9 – Material Response of a rate-sensitive material at Hardening and Softening; (a) Stress-Strain relation at Hardening (at $x=0.5$) at time, $T=0.05$, (b) Plastic Strain field plot at Hardening at time, $T=0.05$, (c) Stress-Strain relation at Softening (at $x=0.5$) at time, $T=0.5$, (d) Plastic Strain field plot at Softening at time, $T=0.5$. *Units: (non-dimensionalized)*

The results were verified on analytical grounds.

In this section, the concept of Damage as an engineering term is introduced and its formulation developed. The results from the Damage theory applied to the same Dynamic 1-D Simple Shear problem are presented.

2.2.2 Damage and Free Energy

Damage may be defined as the nucleation and growth of voids/cracks in a body. It is the primary phenomenon responsible for failure of brittle materials like concrete and rocks.

The following formulation is an excerpt from a paper by Acharya (2009). The major assumptions are:

- The physical body containing voids is thought of as a set of points. Each point is endowed with a void volume fraction attribute, defined physically as the limit of the ratio of the volume of voids in a region to the volume of the region, as the volume of the region goes to zero. The void volume fraction field on the body naturally varies with time. This field is identified as the damage variable of the model, physically representative of a density of microcavity volume in the material. We denote it with the symbol $\varphi \in [0, 1]$.
- The linear elastic moduli, and therefore the specific free energy, of the voided material depends on the void volume fraction. Thus, the specific free energy of the material depends, as a first approximation, only on

elastic strain and the void volume fraction. In particular, the specific free energy of the material does not depend on a gradient of the damage variable.

- The void volume fraction, defined as above, is a volumetric density. Therefore, its evolution can be expressed as a balance law. For, if we focus on any arbitrarily fixed region in the body, it is a purely kinematic argument that the rate of change of the void volume contained in that region changes due to the production of new voids and due to the influx of void volume content from the ingress of microcracks/cavities into that volume from its exterior. It should be carefully noted that a flux of void volume through a surface is not necessarily to be identified with a transport of entire voids through the surface, each void considered as an entity. Instead the expansion/contraction of the voids causes the flux in void volume that is relevant for this discussion. In other words, void transport is sufficient for transport of void volume, but not necessary. Thus, the flux of void volume may be linked to the transport of infinitesimal elements of void- solid interface instead of entire voids.

Let, ψ be the free energy per unit volume and φ being the void volume fraction such that;

$$\psi = \psi(\varphi, \varepsilon)$$

We assume that the dissipated mechanical energy characterized by the rate of working of the external loads less the rate of change of free energy and

kinetic energy of the body is always non-negative in any physical process of the body. If ‘ D ’ is the Energy Dissipation rate (Power), then:

$$D = \left\{ \int_B (\underline{\sigma} : \underline{\dot{\varepsilon}}) dV - \int_B \dot{\psi} dV \right\} \geq 0 \quad (2.8)$$

where, $\underline{\sigma}$ is the stress, $\underline{\varepsilon}$ is the strain, $\underline{\dot{\varepsilon}}$ is the strain rate and $\dot{\psi}$ is the rate of change of free energy per unit volume.

We may expand $\dot{\psi}$ as:

$$\dot{\psi} = \frac{\partial \widehat{\psi}}{\partial \varphi} : \dot{\varphi} + \frac{\partial \widehat{\psi}}{\partial \underline{\varepsilon}} : \underline{\dot{\varepsilon}} \quad (2.9)$$

Assume,

$$\underline{\sigma} = \frac{\partial \widehat{\psi}}{\partial \underline{\varepsilon}} \quad (2.10)$$

Substituting (2.9) and (2.10) in (2.8) we get,

$$D = \left\{ \int_B \left(\frac{\partial \widehat{\psi}}{\partial \underline{\varepsilon}} : \underline{\dot{\varepsilon}} \right) dV - \int_B \left(\frac{\partial \widehat{\psi}}{\partial \underline{\varepsilon}} : \underline{\dot{\varepsilon}} \right) dV - \int_B \left(\frac{\partial \widehat{\psi}}{\partial \varphi} : \dot{\varphi} \right) dV \right\} \geq 0 \quad (2.11)$$

which is an expression of the second law of thermodynamics.

Therefore,

$$D = \left\{ \int_B \left(-\frac{\partial \hat{\psi}}{\partial \varphi} : \dot{\varphi} \right) dV \right\} \geq 0 \quad (2.12)$$

As already mentioned before that the evolution of void-volume fraction can be expressed as a balance law, therefore, void-volume fraction field satisfies

$$\dot{\varphi} = \operatorname{div} \left(\underset{\sim}{f} \right) + s \quad (2.13)$$

where, $\dot{\varphi}$ is the rate of change of void volume fraction and $\underset{\sim}{f} \cdot \hat{n}$ is the inward flux of void-volume through the surface with a unit outward normal \hat{n} .

Substituting (2.13) in (2.12) and using Divergence Theorem, we get:

$$D = \int_B \left[-\operatorname{grad}(Y) \cdot \underset{\sim}{f} \right] dV + \int_B [Ys] dV + \int_{\partial B} \left[Y \underset{\sim}{f} \cdot \hat{n} \right] da \quad (2.14)$$

where, $Y = -\left(\frac{\partial \hat{\psi}}{\partial \varphi} \right)$ is called the damage energy release rate

So, the driving force for $\underset{\sim}{f}$ is $-\operatorname{grad}(Y)$ and the driving force for s is Y .

Also, under constraint, $\int_{\partial B} \left[Y \underset{\sim}{f} \cdot \hat{n} \right] da = 0$, i.e. flux across the boundary is zero.

2.2.2.1 Choosing f and s

Assume,

$$\underline{f} = K (-grad(Y))$$

where, K is a positive scalar given as: Bw and;

$$-grad(Y) = -grad \left(-\frac{\partial \widehat{\psi}}{\partial \varphi} \right) = \left(\frac{\partial^2 \widehat{\psi}}{\partial \varphi^2} \right) (grad(\varphi)) + \left(\frac{\partial^2 \widehat{\psi}}{\partial \varphi \partial \varepsilon} \right) (grad(\varepsilon)) \quad (2.15)$$

For simplicity, we study the following approximation in this work

$$\underline{f} \cong Bw \left(\frac{\partial^2 \widehat{\psi}}{\partial \varphi^2} \right) (grad(\varphi))$$

B is a positive constant for dimensional reasons, $\frac{\partial^2 \psi}{\partial \varphi^2} \geq 0$ implies flux from higher φ to lower φ and w is the damage driving variable.

The damage driving variable w responds based on material behavior. If the local material response is rate-independent, then w ensures that the evolution of void-volume fraction is rate-independent as well. However, for the considered problem as we shall see in the next sub-section the local response is rate-dependent with low material rate-sensitivity, which implies that w ensures a rate-insensitive evolution of void-volume fraction.

The local damage theories usually describe the damage evolution as a function of damage driving variable w . In our model, however, the damage evolution equation has a diffusion part plus a source term s . The diffusion part is an outcome of non-local material response. This prompts us to think that

the derived local setting from our equation should match the classical local damage evolution. Based on this reasoning, the source term is given by the following expression:

$$s = \text{sign}(Y) w \quad (2.16)$$

The second term in the expression for $\text{grad}(Y)$ in equation 2.15 can be considered as a candidate for a source term s . However, in the present case, we make the more conventional choice (equation 2.16).

2.2.3 Dynamic 1-D Simple Shear Problem

We consider exactly the same problem as introduced in section 2.1 with the same initial and boundary conditions. The governing equations for the Damage Formulation are a set of coupled equations, namely:

- Balance of Linear Momentum equation: $\rho \dot{v} = \sigma_{,x}$
- Damage Evolution equation: $\dot{\varphi} = \text{div} \left(\underset{\sim}{f} \right) + s$

The symbols have their usual meanings.

The expressions for free energy (ψ), damage energy release rate (Y), damage threshold ($G(\varphi)$) and damage driving variable (w) respectively are given below:

Free Energy expression, $\psi(\hat{\varphi}, \varepsilon)$:

$$\widehat{\psi}(\varphi, \varepsilon) = \frac{1}{2} \left[1 - \left(1 + \frac{e_c}{2} \right) \varphi + \frac{e_c}{2} \varphi^2 \right] \psi_{\text{undamaged}} \quad (2.17)$$

where, $\psi_{\text{undamaged}} = \mu \varepsilon^2$ (μ - shear modulus) and e_c is a small positive dimensionless constant (equal to 0.001).

The constant e_c helps lend a material length scale to the model. The expression for $\left(\frac{\partial^2 \psi}{\partial \varphi^2} \right)$ is given as:

$$\frac{\partial^2 \psi}{\partial \varphi^2} = \psi_{\text{undamaged}} e_c$$

With e_c positive and non-zero, we have $\frac{\partial^2 \psi}{\partial \varphi^2} \geq 0$ (convexity) i.e. flux from higher φ to lower φ . Then, the length scale enters the problem through the whole diffusion coefficient β , which is:

$$\beta = Bw \left(\frac{\partial^2 \psi}{\partial \varphi^2} \right)$$

Damage Energy Release rate, $Y = - \left(\frac{\partial \widehat{\psi}}{\partial \varphi} \right)$:

$$Y = \frac{1}{2} \left[\left(1 + \frac{e_c}{2} \right) - e_c \varphi \right] \psi_{\text{undamaged}} \quad (2.18)$$

Damage Threshold (Bažant and Pijaudier-Cabot 1988), $G(\varphi)$:

$$G(\varphi) = \frac{(1 - \varphi)^{\frac{1}{\vartheta}} - 1}{b} + Y_1 \quad (2.19)$$

where, ϑ and b are positive material constants ($\vartheta > 2$) and Y_1 is local damage threshold.

Damage Driving variable, w :

$$w = w_0 \left(\frac{Y}{G(\varphi)} \right)^{\frac{1}{m}} \quad (2.20)$$

where, w_0 is a constant which depends on strain rate and m is rate sensitivity.

Finally, stress $\left(\sigma = \frac{\partial \hat{\psi}}{\partial \varepsilon} \right)$ is given by the following expression:

$$\sigma = \mu \varepsilon \left[1 - \left(1 + \frac{e_c}{2} \right) \varphi + \frac{e_c}{2} \varphi^2 \right] \quad (2.21)$$

The Damage problem is solved numerically using the explicit Finite Element technique for the coupled equations. Finite element method is preferred over the Finite difference method since FEM provides a natural handling of discontinuities, which arise due to damage.

Solving the Balance of Linear Momentum equation gives an update of displacement and in turn strain. The void-volume fraction is updated by solving the Damage Evolution equation. The equations are coupled in the sense that both the strain and the void-volume fraction increments are required to update the stress. It is clearly seen in the stress calculation equation 2.21.

The time-step is taken as the minimum of the:

- Time-step determined from the Courant condition (balance of linear

momentum equation or the wave equation): $C_s \Delta t_{wave} \leq \Delta x$, where,

$$C_s = \sqrt{\frac{\mu}{\rho}}$$

- Time-step determined from the stability of the Damage Evolution equation: $\Delta t_d \leq \left(\frac{(\Delta x)^2}{2\beta}\right)$, where, $\beta = Bw \left(\frac{\partial^2 \psi}{\partial \varphi^2}\right)$ is the diffusion coefficient

2.2.3.1 Verifying the Damage Evolution equation:

The Damage evolution equation is a nonlinear diffusion equation with a diffusion term, $div(f)$ and a source term, s . The property of the heat equation is that, it diffuses an initial variable in the form of a delta function with a certain rate of diffusion depending upon the diffusion coefficient of the equation.

Here, the source term was ignored and the diffusion coefficient kept constant. Figure 2.10 shows how diffusion equation smoothes out the solution progressively over a period of time. The numerical and analytical solutions at the same time were found to be equal.

2.2.3.2 Results

The results corresponding to the response of the material under dynamic loading are presented. The material was assumed to be non-homogeneous with void-volume fraction profile as a smooth Gaussian as shown in Figure 2.13. The material has 1% voids at the center.

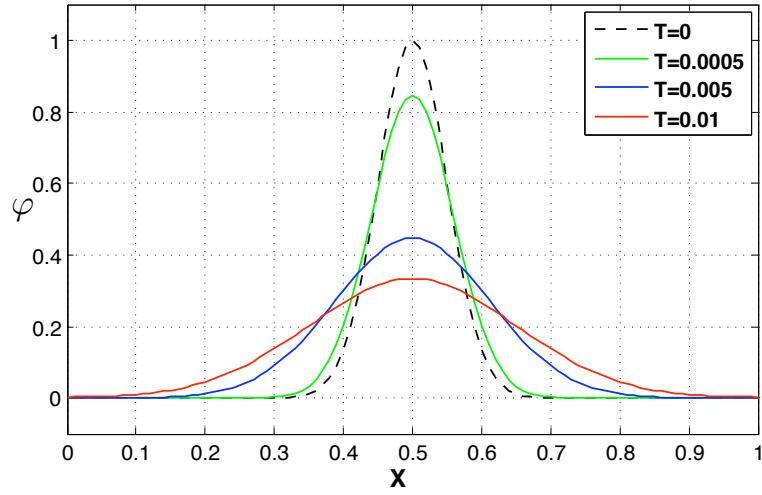


Figure 2.10 – Verification result for the Damage Evolution equation. *Units: distance (m)*

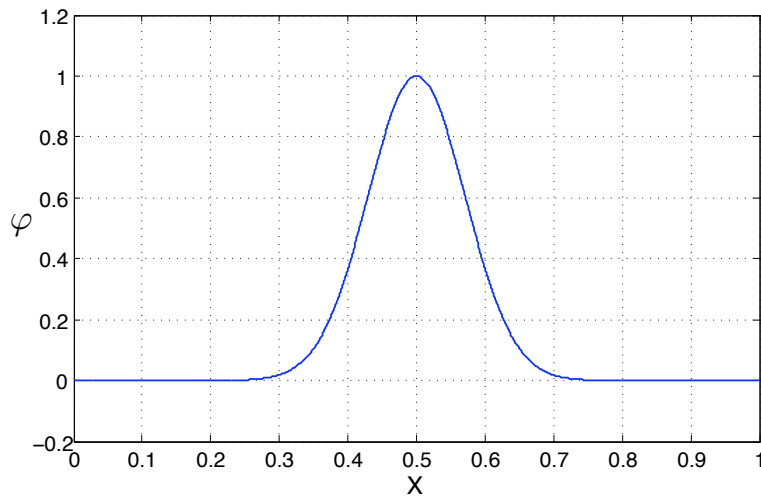


Figure 2.11 – Initial condition on void-volume fraction (in %). *Units: distance (m)*

The other initial conditions are:

- Initial condition on displacement, $u_0 = 0$
- Initial condition on velocity, $v_0 = 0$

The results here are presented for the non-local case only. For the local case, the solution converged more like the non-local case, owing to the rate-dependent scheme employed.

The damage evolution equation $\dot{\varphi} = \text{div} \left(\underset{\sim}{f} \right) + s$, can be written in the following form:

$$\dot{\varphi} = Bw \left(\frac{\partial^2 \psi}{\partial \varphi^2} \right) \left(\frac{\partial^2 \varphi}{\partial x^2} \right)$$

For the local case, we equate $B = 0$, therefore, ending up with the governing equation for the local case:

$$\dot{\varphi} = s$$

Figure 2.12 shows results for the non-local case. Mesh size independence is clearly visible at and beyond softening and the solution is a convergent one owing to the stabilizing effect of the non-local behavior. The mesh refinements of 200, 1000 and 2000 elements respectively were used.

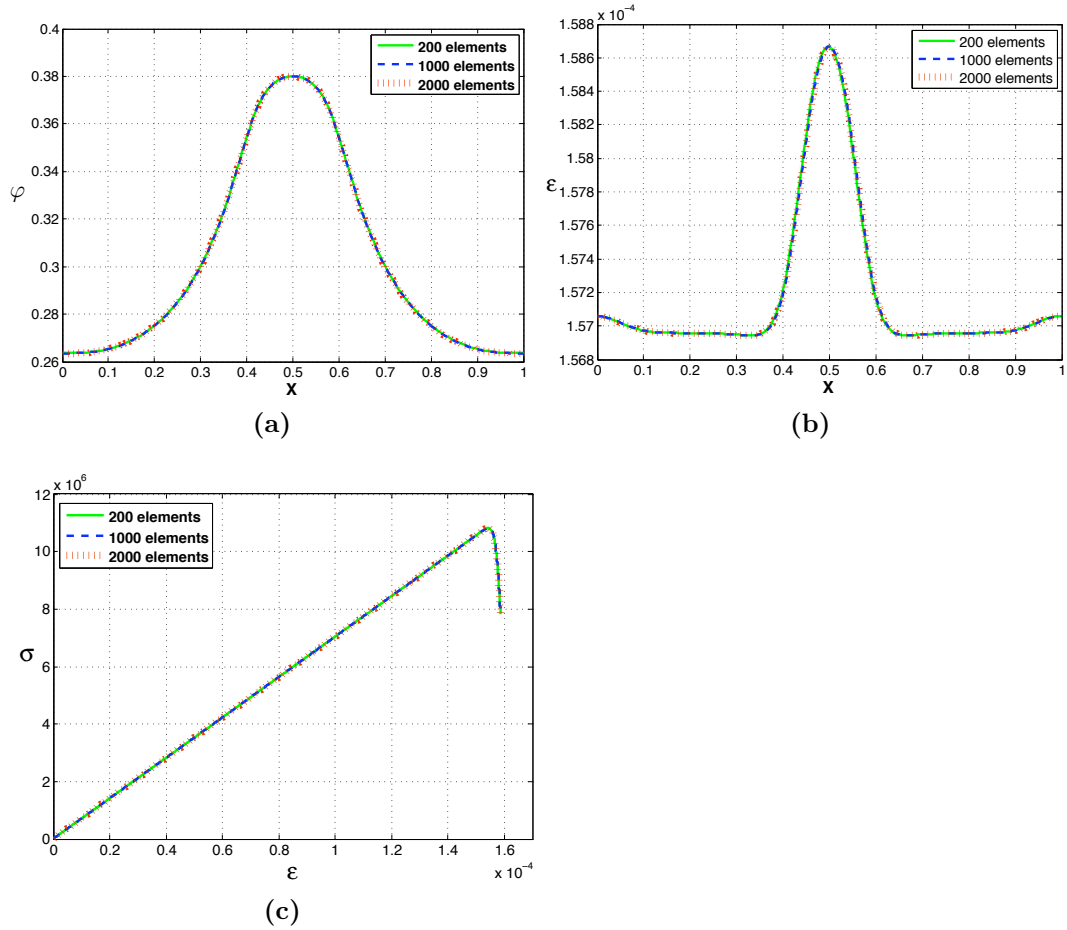


Figure 2.12 – Results for the Non-Local case after softening; (a) Field plot of Void-volume fraction, (b) Field plot of Strain, (c) Stress-Strain relation at the center. *Units: distance (m), stress (N/m²)*

2.3 Ductile/Plastic Damage (1-D)

2.3.1 Introduction

The Ductile Damage Model is similar to the Damage Model formulated earlier. However, it is assumed that the Damage is controlled and driven by Plasticity. The material response chosen here even though appropriate for damage modeling in metals is a reasonable choice for our numerical modeling of rock damage coupled with plasticity. A Rock, which is otherwise a brittle material, behaves more like a metal showing ductile behavior under the conditions of HPHT. Due to confinement the fragments can stay together and flow like a continuum thus demonstrating ductile behavior.

The governing equations remain the same as for a pure damage model. For sake of convenience, the governing equations are given below:

- Balance of Linear Momentum equation:

$$\rho \dot{v} = \sigma_{,x} \quad (2.22)$$

- Damage Evolution equation:

$$\dot{\varphi} = \text{div} \left(\underset{\sim}{f} \right) + s \quad (2.23)$$

The terms f and s are chosen as follows:

$$\tilde{f} = Bw \left(\frac{\partial^2 \widehat{\psi}}{\partial \varphi^2} \right) \left(\frac{\partial \varphi}{\partial x} \right) \quad (2.24)$$

$$s = \text{sign}(Y) w \quad (2.25)$$

The symbols have their usual meaning as already mentioned above.

The total strain ε is given by:

$$\varepsilon = \frac{\partial u}{\partial x} \quad (2.26)$$

where, u is the displacement.

If ε^p is the plastic strain, then elastic strain ε^e is given as:

$$\varepsilon^e = \varepsilon - \varepsilon^p \quad (2.27)$$

The stress is then determined by differentiating the free energy expression with respect to the elastic strain as:

$$\sigma = \frac{\partial \widehat{\psi}(\varphi, \varepsilon^e)}{\partial \varphi} = \mu \varepsilon^e \left[1 - \left(1 + \frac{e_c}{2} \right) \varphi + \frac{e_c}{2} \varphi^2 \right] \quad (2.28)$$

And, the Damage Driving variable, w is given by (Mediavilla, J. etal, 2006):

$$w = \left[\left\langle 1 + A \frac{\tau_h}{\tau_{eq}} \right\rangle (\varepsilon^p)^\kappa \right] (\dot{\varepsilon}^p) \quad (2.29)$$

where, A and κ are material constants, τ_h is hydrostatic stress, τ_{eq} is effective stress and $\langle \bullet \rangle$ are Macaulay brackets, such that: $\langle x \rangle = \frac{1}{2}(x + |x|)$.

The damage driving variable w affects how the void-volume fraction is generated and is shown to be realistically dependent on hydrostatic pressure and plastic strain rate. The dependence on plastic strain rate implies that damage is driven by plasticity. In the 1D simulations, w was determined individually for each gauss point of each element, of course from the plastic strain rate. However, as we shall see later, it is not the case in 3D rock indentation problem. It is required that a spatially uniform damage driving variable be used in the diffusion part. The need and explanation is given in Chapter 5 (section 5.4).

2.3.2 Dynamic 1-D Simple Shear Problem

We again consider the same problem as introduced in section 2.1 with the same initial and boundary conditions.

At time ' t ', we have:

- Displacement, u
- Void-volume fraction, φ
- The total strain, plastic strain and elastic strain (from equation 2.27)
- Knowing the elastic strain, we can calculate stress using equation 2.28

After calculating stress, the check for plasticity is made as:

$$y = |\sigma| - \tau \quad (2.30)$$

where τ , is the flow stress and is given by: $\tau = \widehat{\tau} (1 - \varphi)$

Algorithm 2.1 One-dimensional Plastic Damage

Case 1: : If $y < 0$, then (there is No Damage but only elastic deformation)

$$w = 0$$

Case 2: : If $y \geq 0$, then (there is Plasticity and Damage)

$$\dot{\gamma} = \left(\frac{\sigma}{\tau} \right)^{\frac{1}{m}} \quad (2.31)$$

$$\Delta\gamma = \Delta t (\dot{\gamma}) \quad (2.32)$$

$$\varepsilon^p = \varepsilon^p + \Delta\gamma \quad (2.33)$$

$$\widehat{\tau} = \widehat{\tau} + H(\varepsilon) \Delta\gamma \quad (2.34)$$

$$w = \left[\left\langle 1 + \frac{\tau_h}{\tau_{eq}} \right\rangle (\varepsilon^p)^\kappa \right] (\dot{\varepsilon}^p) \quad (2.35)$$

$H(\varepsilon^p)$ is the hardening function. Here, we choose a different hardening expression relevant to the ductile damage model given by (Mediavilla, J. etal, 2006):

$$H(\varepsilon^p) = h_p + \zeta (\tau_{y\infty} - \tau_{y0}) (e^{-\zeta \varepsilon^p}) \quad (2.36)$$

In the above expression, h_p is linear hardening coefficient, ζ is saturation exponent, $\tau_{y\infty}$ is residual flow stress and τ_{y0} is initial flow stress.

The information above is used to update strain, void volume fraction and stress in the following manner:

- Solving the balance of linear momentum equation updates displacement.
- Solving the damage evolution equation, the void-volume fraction is updated.

The total strain, elastic strain and stress are updated equations 2.26, 2.27 and 2.28 respectively.

2.3.2.1 Results

The following two cases are considered:

- Local Case
- Non-Local Case

This is followed by comparison of the local and non-local results. Figure 2.13 shows the initial condition on the void-volume fraction used for both the above-mentioned cases.

Local Case

As mentioned in the previous section, the damage evolution equation $\dot{\varphi} = \text{div} \left(\underset{\sim}{f} \right) + s$, can be written in the following form:

$$\dot{\varphi} = Bw \left(\frac{\partial^2 \psi}{\partial \varphi^2} \right) \left(\frac{\partial^2 \varphi}{\partial x^2} \right)$$

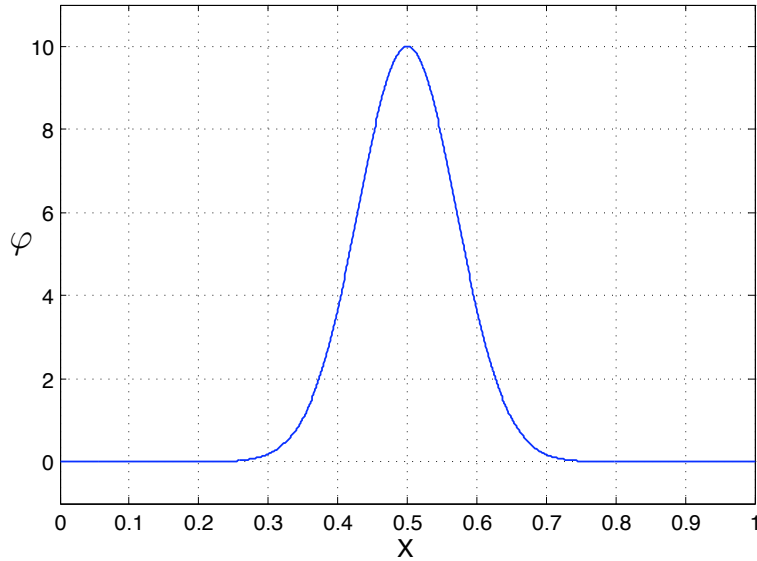


Figure 2.13 – Initial condition on void-volume fraction (in %). *Units: distance (m)*

For the local case, we equate $B = 0$, therefore, ending up with the governing equation for the local case:

$$\dot{\varphi} = s$$

The results for the local case are shown in Figure 2.14. The mesh refinements used were 100, 1000, 2000 and 5000 elements respectively. The results corresponding to each mesh size were plotted at the same physical time. It is clear from the results that there is mesh size dependence. As the mesh size is decreased, there is localization of void-volume fraction field plot and the strain field plot. The stress-strain response at the center of the specimen also shows a varied response with mesh refinement. Therefore, we do not have a convergent solution for the local setting.

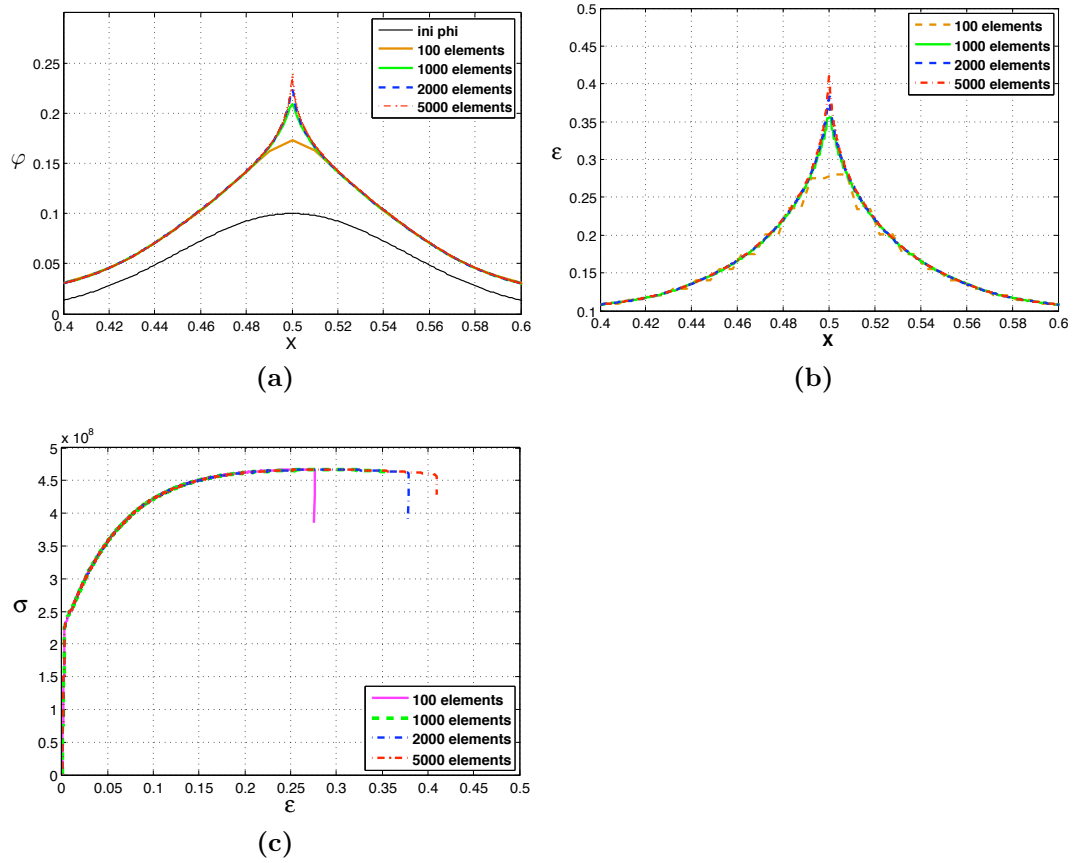


Figure 2.14 – Results for the Local Case; (a) Field plot for void-volume fraction, (b) Field plot for strain, (c) Stress-Strain relation at the center. *Units: distance (m), stress (N/m²)*

Non-Local Case

The results for the non-local case are shown in Figure 2.15. The mesh refinements used were 100, 500 and 1000 elements respectively. The results are plotted at the same physical time. It is clear from the results that there is mesh size independence as the results derived from all the mesh sizes converge to the same solution. Therefore, we have a convergent solution for the non-local setting.

Local vs Non-Local Results

In order to appreciate the stabilizing behavior of the non-local scheme compared to the local scheme, we compare the respective results at the same physical time. The comparison is shown in Figure 2.16 with respect to field plots for void-volume fraction and strain and stress-strain plots at the center of the material.

A more stable behavior of the non-local scheme is clear from Figure 2.16. The stress-strain curves separate with the non-local curve going over the local curve. Since the comparison is made at the same physical time, the local curve has reached failure whereas the non-local curve is still in hardening.

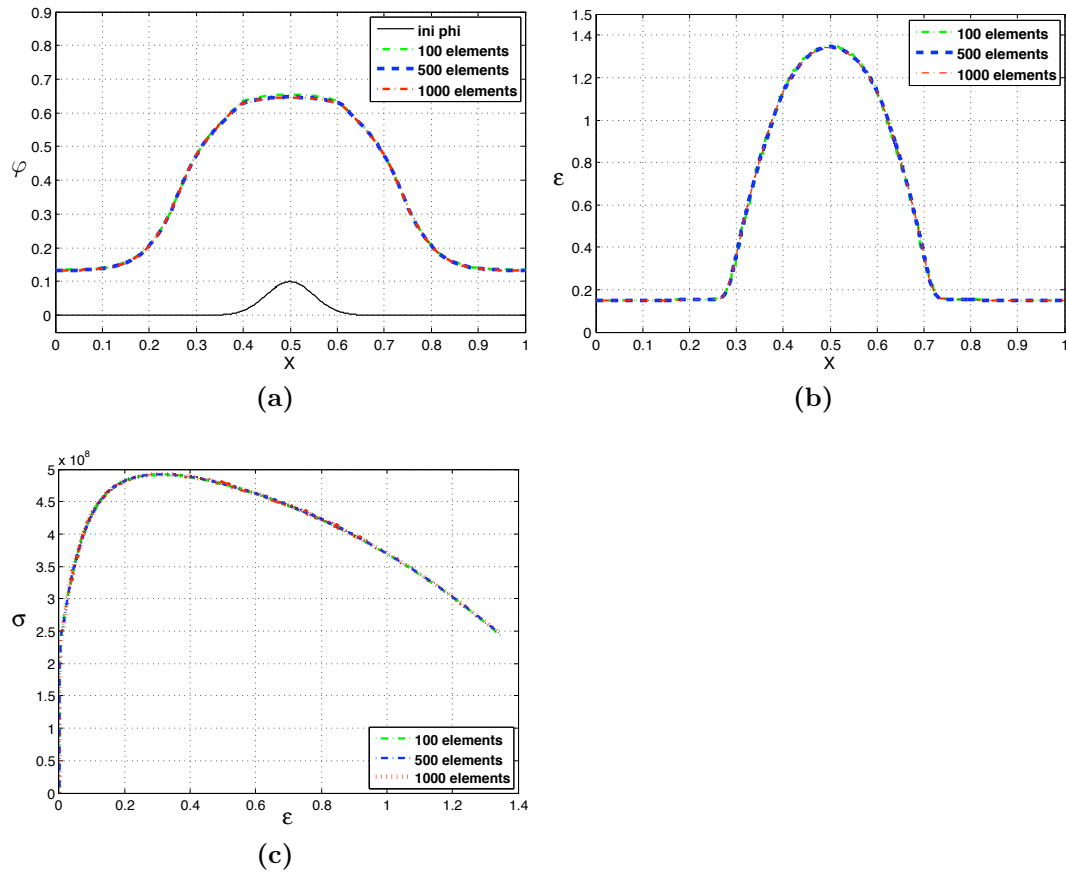


Figure 2.15 – Results for the Non-local case; (a) Field plot for void-volume fraction, (b) Field plot for strain, (c) Stress-Strain relation at the center. *Units: distance (m), stress (N/m²)*

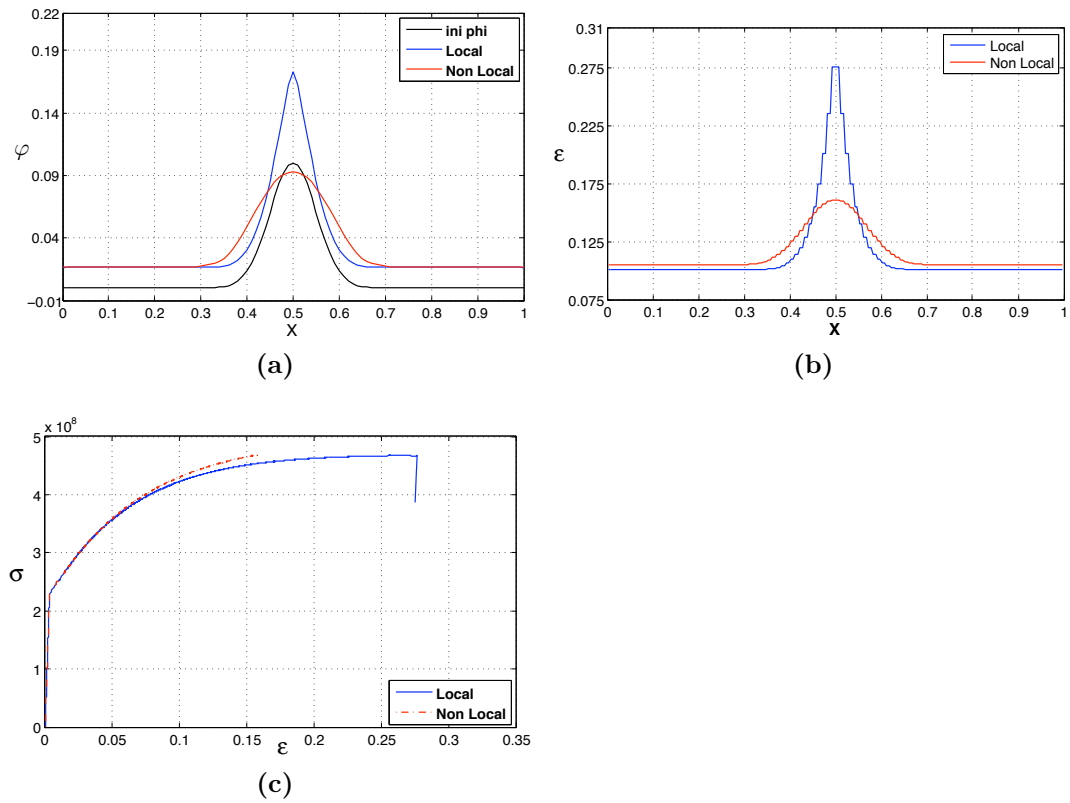


Figure 2.16 – Comparison between Local and Non-Local results; (a) Field plot for void-volume fraction, (b) Field plot for strain, (c) Stress-Strain curves. Units: distance (m), stress (N/m^2)

Chapter 3

3D Ductile Damage

3.1 Introduction

The main purpose of this research is to develop a 3D non-local macroscopic model of combined brittle-ductile damage that allows us to model the behavior of rocks under HPHT conditions. The importance of non-locality can be inferred from the results of 1D non-local analysis (presented earlier) where we noticed mesh size independence and stability. We want to extend this concept into 3D analyses as well.

The plasticity model used is Drucker-Prager model (Drucker and Prager 1952). Drucker-Prager model is a pressure dependent model and has been traditionally used for geomaterials (Salari, M.R etal 2004). Hence its qualification was obvious. It is however important to mention here that the Drucker-Prager

model is only one and the first possible candidate for Rock failure. Our code is modular and can incorporate other models instead of Drucker-Prager model for the Damage Driving variable determination.

Further, real rock data is required so that the resulting model has a desired realistic basis.

3.2 Generalized Drucker-Prager Plasticity Model

The Drucker-Prager model (Drucker and Prager 1952) is a Classical Plasticity model used in case of soils and rocks. It and its many variants have been applied to rock, concrete, polymers, foams, and other pressure-dependent materials.

The model is an isotropic elasto-plastic model based on a yield function:

$$y(\underline{\sigma}, e^p) = \Gamma(\sigma) - H(e^p)$$

where, $\Gamma(\sigma) = \chi - \alpha p$, σ is stress tensor, $H(e^p)$ is hardening function, p is pressure given by: $-\frac{1}{3}tr(\sigma)$, $\chi = \sqrt{\frac{1}{2}\underline{\sigma}' : \underline{\sigma}'}$, $\underline{\sigma}'$ is deviatoric stress and α is positive friction coefficient, which controls the influence of pressure on the yield limit.

The plastic potential $g(\sigma)$ is given by:

$$g(\sigma) = \chi - \alpha_\psi p$$

where, α_ψ is dilatancy constant.

Now, the plastic strain rate is given by:

$$\underline{\dot{\epsilon}}^p = v \frac{\partial g}{\partial \underline{\sigma}}$$

where, $\frac{\partial g}{\partial \underline{\sigma}} = \frac{\alpha_\psi^2}{3} \underline{I} + \frac{1}{2\chi} \underline{\sigma}'$

Also,

$$\dot{e}^p = \left| \underline{\dot{\epsilon}}^p \right| = v \left| \frac{\partial g}{\partial \underline{\sigma}} \right|$$

where, $\left| \frac{\partial g}{\partial \underline{\sigma}} \right| = \sqrt{\frac{\alpha_\psi^2}{3} + \frac{1}{2}} = \eta$ and $v = \frac{\dot{e}^p}{\left| \frac{\partial g}{\partial \underline{\sigma}} \right|}$

Therefore,

$$\underline{\dot{\epsilon}}^p = \frac{\dot{e}^p}{\eta} \frac{\partial g}{\partial \underline{\sigma}}$$

and

$$\dot{e}^p = \left(\frac{f(\underline{\sigma})}{H(e^p)} \right)^{\frac{1}{m}}$$

m - is rate sensitivity

3.3 3D Non-Local Ductile Damage

The various equations in 3D take the following form:

- Balance of Linear Momentum Equation (please note that we are neglecting body force density): $\rho \ddot{u}_i = \sigma_{ij,j}$

- Damage evolution equation, also called as the Void-Volume Fraction

$$\text{Equation: } \dot{\varphi} = \text{div} \left(\underset{\sim}{f} \right) + s$$

ρ is mass desity, u is displacement, σ is stress, φ is void-volume fraction, $\underset{\sim}{f} \cdot \hat{n}$ is the inward flux of the void-volume through the surface with a unit outward normal, \hat{n} and s is source term.

$$f_j = Bw \left(\frac{\partial^2 \hat{\psi}}{\partial \varphi^2} \right) \left(\frac{\partial \varphi}{\partial x_j} \right)$$

where, B is a positive constant for dimensional purposes, w is damage driving variable and ψ is free energy.

The expressions for the damage driving variable, the free energy, the stress and the yield equation respectively are:

- Damage driving variable: $w = \left[\left\langle 1 + A \frac{\tau_h}{\tau_{eq}} \right\rangle (e^p)^\kappa \right] (\dot{e}^p)$
- Free Energy: $\hat{\psi}(\varphi, \underline{\varepsilon}^e) = \frac{1}{2} C_{ijkl} (\varepsilon_{ij} - \varepsilon_{ij}^p) (\varepsilon_{kl} - \varepsilon_{kl}^p) \left[1 - \left(1 + \frac{e_c}{2} \right) \varphi + \frac{e_c}{2} \varphi^2 \right]$
- Stress: $\sigma_{ij} = C_{ijkl} (\varepsilon_{kl} - \varepsilon_{kl}^p) \left[1 - \left(1 + \frac{e_c}{2} \right) \varphi + \frac{e_c}{2} \varphi^2 \right]$
- Yield equation: $\tau = \hat{\tau} (1 - \varphi)$

In the above expressions; $\underline{\varepsilon}^e$ is elastic strain, $\underline{\varepsilon}^p$ is pastic strain, A , κ and e_c are material constants, τ_h is hydrostatic pressure, τ_{eq} is effective stress, τ is flow stress and \underline{C} is modulus.

The damage driving variable affects how the void-volume fraction is generated and is shown to be realistically dependent on hydrostatic pressure. In the

present case, i.e for the current model, it is dependent on Plastic Straining.

3.3.1 Solving Scheme

For time t , we have the following information:

- Void-volume fraction, φ_t
- Total strain, $(\varepsilon_{ij})^t$
- Elastic strain, $(\varepsilon_{ij}^e)^t$
- Stress: $\sigma_{ij}^t = C_{ijkl} ((\varepsilon_{kl})^t - (\varepsilon_{kl}^e)^t) [1 - (1 + \frac{e_c}{2}) \varphi_t + \frac{e_c}{2} \varphi_t^2]$
- Yield stress: $\tau_t = \hat{\tau}_t (1 - \varphi_t)$

For time $= t + \Delta t$: (where, Δt is the time step) we start with the plasticity check and follow steps in Algorithm 3.1

$$y(\underline{\sigma}, e^p) = \Gamma(\sigma) - \tau$$

$H(\varepsilon^p)$ is the hardening function given by:

$$H(\varepsilon^p) = h_p + \zeta (\tau_{y\infty} - \tau_{y0}) (e^{-\zeta \varepsilon^p}) \quad (3.1)$$

In the above expression, h_p is linear hardening coefficient, ζ is saturation exponent, $\tau_{y\infty}$ is residual flow stress and τ_{y0} is initial flow stress.

Now, we have all the information required to update strain, void-volume fraction and stress in the following manner:

Algorithm 3.1 Working mechanism for 2D/3D Non-local ductile damage

IF $y(\underline{\sigma}, e^p) < 0$, then - Elastic Step (No Damage)

- $(\varepsilon_{ij}^p) = (\varepsilon_{ij}^p)^t$
- $\widehat{\tau} = \widehat{\tau}_t$
- $w = 0$

IF $y(\underline{\sigma}, e^p) \geq 0$, then - Plastic Step (Damage)

- Compute the plastic multiplier, $\dot{\gamma}$
- Compute the updated plastic strain: $(\varepsilon_{ij}^p) = (\varepsilon_{ij}^p)^t + \Delta t \dot{\gamma} \frac{\sigma'_{ij}}{|\sqrt{\sigma'_{ij} \cdot \sigma'_{ij}}|}$
- Compute the updated flow stress: $\widehat{\tau} = \widehat{\tau}_t + H(e^p) \Delta \gamma$, where $\Delta \gamma = \Delta t \dot{\gamma}$
- Compute the damage driving variable: $w = \left[\left\langle 1 + A \frac{\tau_h}{\tau_{eq}} \right\rangle (e^p)^\kappa \right] (\dot{e}^p)$

With these updates, we can compute residual vectors containing nodal values for the balance of linear momentum and the damage evolution equations respectively.

- Solving the Finite Element form of the balance of linear momentum equation, we get updated displacements at nodes
- Solving the Finite Element form of the damage evolution equation, we get updated values of void-volume fraction at nodes

With all the above updates we may update our stress using the equation already introduced above and written here again for convenience:

$$\sigma_{ij} = C_{ijkl} (\varepsilon_{kl} - \varepsilon_{kl}^p) \left[1 - \left(1 + \frac{e_c}{2} \right) \varphi + \frac{e_c}{2} \varphi^2 \right]$$

3.4 Verification of the 3D model

Once the above set of equations is coded up and the model framed, it is important to verify the model in all possible aspects. As in the 1D case, we shall verify the governing equations first with numerical tools and analytical results available. Again, the idea is to deactivate one of the governing equations while verifying the other and vice versa.

3.4.1 Verification of the Governing Equations

A 3D block considered for the verification of governing equations is shown in Figure 3.1 below.

Boundary Conditions: displacement in x-direction (u_1) = 0 at left back and front bottom corners.

Initial Conditions: u_1 in the form of a Gaussian with its peak at the center and zero towards ends.

Constraints: $u_2 = u_3 = 0$

The Damage equation was deactivated while the Balance of Linear Momentum equation was being verified. The Damage equation is deactivated by forcing the void-volume fraction to zero at all times, while the Linear Momentum equation stays active with only ' x ' degrees of freedom.

The balance of linear momentum equation generates a wave motion, which for a homogeneous linear elastic material must satisfy the classical D'Alembert

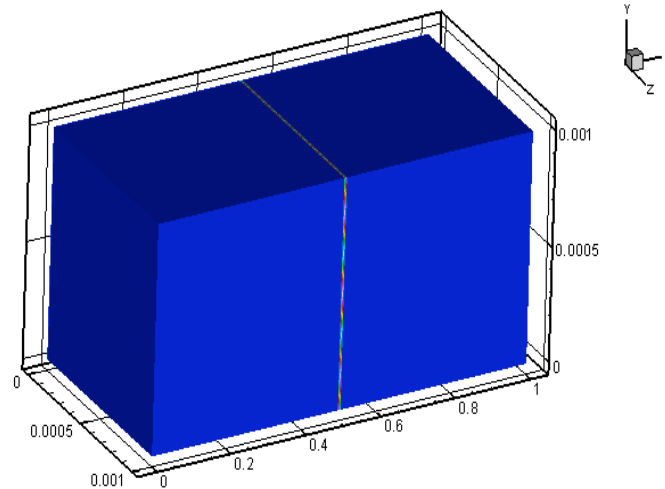


Figure 3.1 – Three dimensional block used for verifying the governing equations. *Units: distance (m)*

solution. Figure 3.2 shows the initial and other states at different times respectively. The calculated and actual velocities were found to be the same as well. The initial perturbation in displacement was provided in the form of a smooth Gaussian only in x -direction (or direction – 1) keeping its value zero in the ‘ y ’ and ‘ z ’ directions respectively. Also, the prescribed initial velocity was set equal to zero. The time-step was also calculated using the Courant condition.

After the verification of the Balance of Linear Momentum equation, it was deactivated while the Damage equation was being verified. The Balance of Linear Momentum equation is deactivated by forcing the displacement to zero at all times, while the Damage equation stays active with only ‘ x ’ degrees of freedom. The Damage evolution equation is basically a heat equation with a

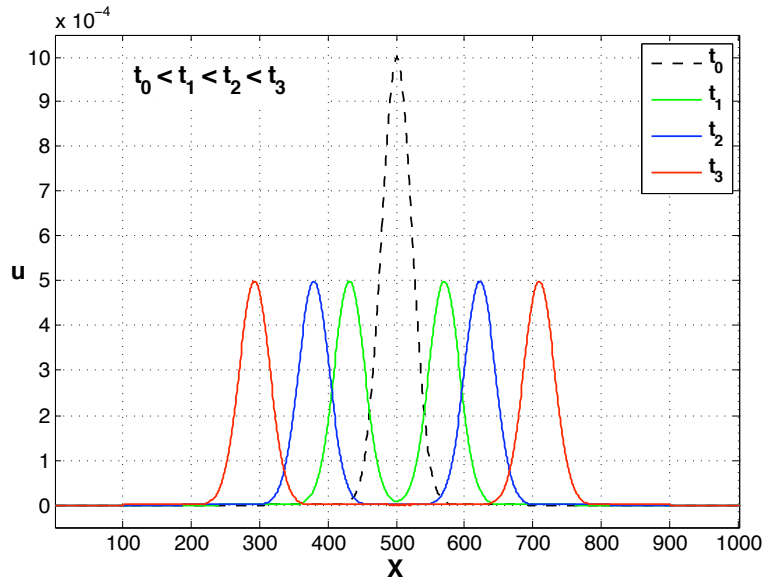


Figure 3.2 – Wave equation verification - Result for only one layer of nodes.
Units: distance (m), displacement (m)

diffusion term, $div(f)$. The property of the heat equation is that, it diffuses an initial profile in the form of a delta function with a certain rate of diffusion depending upon the diffusion coefficient of the equation. Figure 3.3 shows the initial and other states at different times respectively.

The initial void-volume fraction was provided in the form of a smooth Gaussian.

3.4.2 Verification of the 3D model

The 3D model was verified taking into consideration the following:

- Simple Shear problem

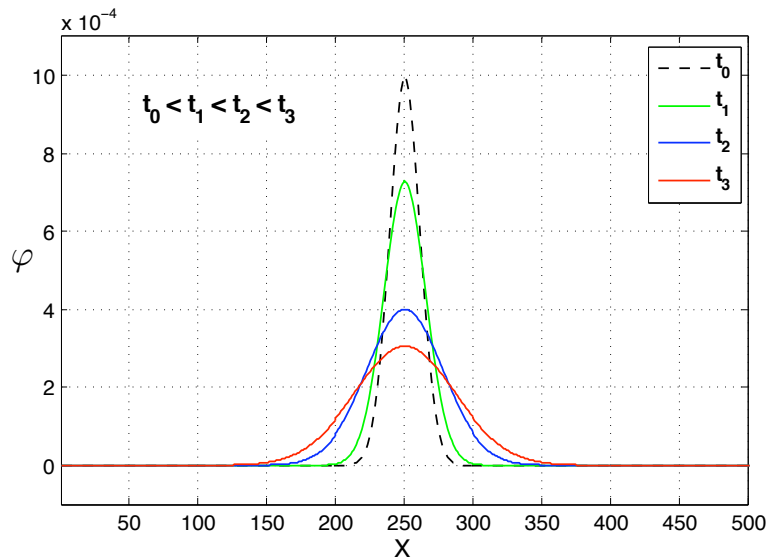


Figure 3.3 – Diffusion equation verification - Result for only one layer of nodes. *Units: distance (m)*

- 3D verification (Elasticity only)
- 3D verification of the J2 Plasticity model (Elasto-plasticity only)
- 3D verification of the Drucker-Prager Plasticity model (Elasto-plasticity only)
- 3D verification of the above models with void-volume fraction active (Elasto-plasticity and damage)
- **Tension problem**
 - 3D verification (Elasticity only - laterally free and laterally constrained cases)
 - 3D verification of the J2 Plasticity model (Elasto-plasticity only)

- 3D verification of the Drucker-Prager Plasticity model (Elasto-plasticity only)
- 3D verification of the above models with void-volume fraction active (Elasto-plasticity and damage)

Key: For this section:

- Directions x , y and z are represented as numbers ‘1’, ‘2’ and ‘3’ respectively.
- Faces of the cube (Figure 3.4)
 - Faces in the $x - y$ plane – front and back
 - Faces in the $y - z$ plane – left and right
 - Faces in the $x - z$ plane – bottom and top

The void-volume equation is kept “inactive” to initially verify the pure elastic and elasto-plastic problems. Further, there is an inertia term in the balance of linear momentum equation ($\rho \ddot{u}_i$), so verification might be difficult. Therefore, it is preferable to transform the dynamic problem into a quasi-static one whose analytical solution/outcome is already known.

A solution for velocity independent of time is assumed to begin with. With velocity independent of time, the stress distribution is uniform and we approach to a quasi-static solution. This solution is used to deduce velocity and displacement initial and boundary conditions for the problem under consideration. The numerical output should match the known analytical

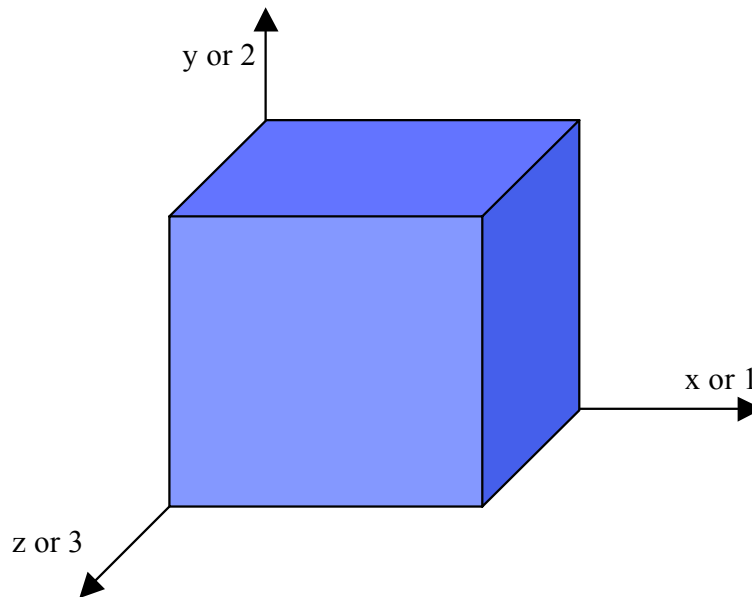


Figure 3.4 – Cube Specimen

result for that problem.

After the elastic and elasto-plastic problems are verified, the void-volume fraction equation is made active. However, the void-volume growth is controlled by a constant value after each increment at the onset of plasticity. This is because of our assumption that the damage variable is driven by plasticity. The stress equation in the analytical case is also modified to accommodate the contribution from void-volume fraction. This is followed by plotting and comparing average-strain versus average-stress corresponding to numerical and analytical cases respectively.

3.4.3 Simple Shear Problem

A cube with each of its sides equal to $1m$ is considered. The boundary and initial conditions are applied in such a way so as to design a problem as if it were a static problem. The analytical results for a static problem are known and can be compared to the numerical results, thereby, verifying the model on this platform for this specific problem.

Boundary Conditions:

- All faces, displacements in 2 and 3 directions, $u_2 = u_3 = 0$
- Bottom face, $u_1 = 0$
- Top face, $u_1 = LT$ (where, L is the height of the cube = $1m$ and T is the total time of run)

Initial Conditions:

- Displacements, $u_1 = u_2 = u_3 = 0$
- Velocities, $v_1(X) = X(x_2)$ (where, X is the position vector and x_2 is the coordinate in 'y' or '2' direction)

3.4.3.1 Verifying the 3D Elastic response

The final average stress versus average strain graph should be a straight line with the slope of the curve equal to the 'shear modulus'. Figure 3.5 shows the plot for the verification of the 3D material model.

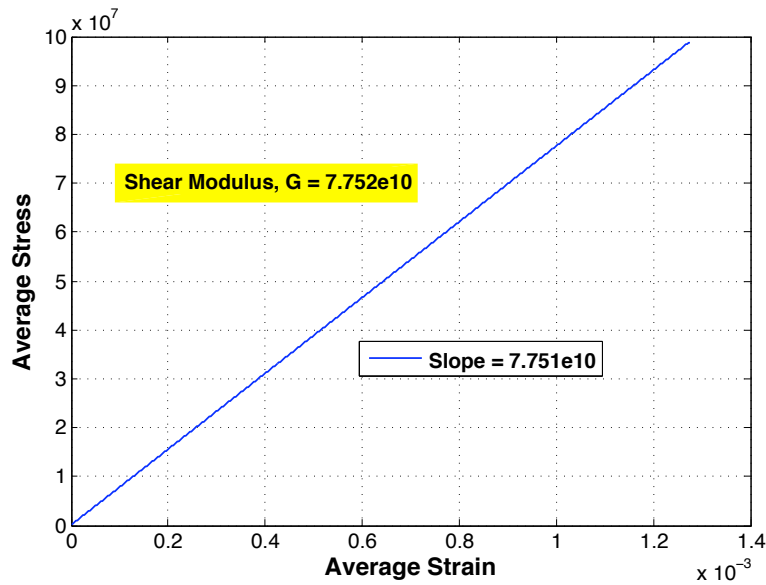


Figure 3.5 – Elasticity verification – Simple Shear. *Units: stress (N/m^2)*

3.4.3.2 Verifying the 3D Elasto-plastic response

Figures 3.6 and 3.7 show comparison between analytical and numerical results for the J2 plasticity and the Drucker-Prager plasticity cases respectively. It is clearly observed that the numerical and analytical results match.

3.4.3.3 Verifying the 3D response for coupled Elasto-plasticity and damage

Figures 3.8 and 3.9 show comparison between analytical and numerical results for the J2 plasticity and the Drucker-Prager plasticity cases with void-volume fraction contribution respectively. As expected, material softening is observed and also the numerical and analytical results match.

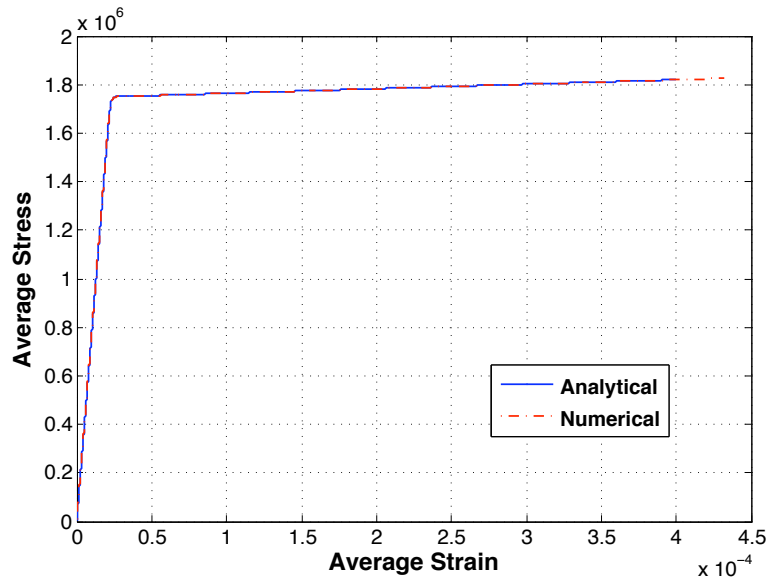


Figure 3.6 – Plasticity verification – Simple-Shear (J2). *Units: stress (N/m^2)*

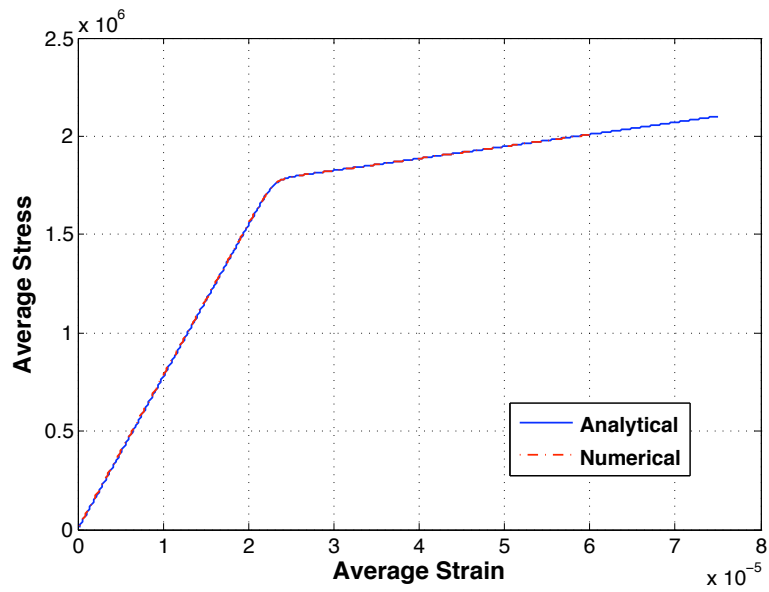


Figure 3.7 – Plasticity verification – Simple-Shear (Drucker-Prager). *Units: stress (N/m^2)*

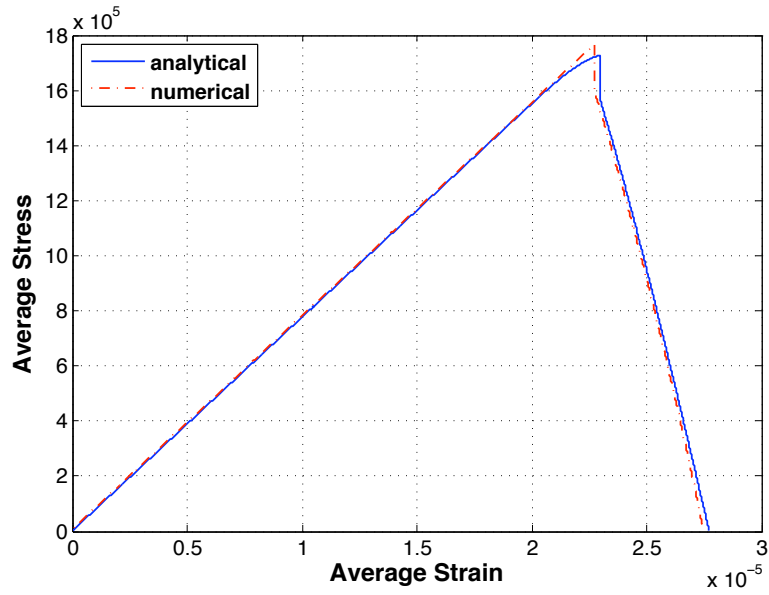


Figure 3.8 – Material softening with damage (J2). Units: stress (N/m^2)

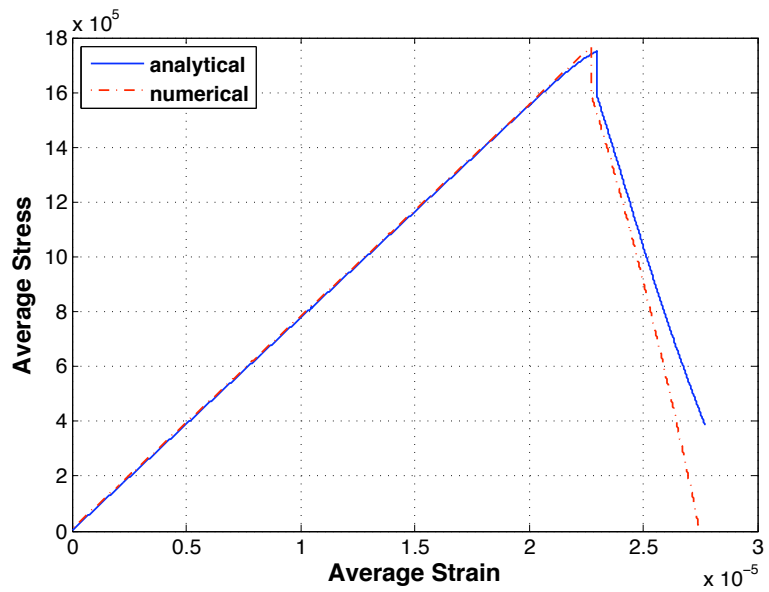


Figure 3.9 – Material softening with damage (Drucker-Prager). Units: stress (N/m^2)

3.4.4 Tension Problem

As in the simple shear problem, a cube with each of its sides equal to $1m$ is considered. The boundary and initial conditions are applied in such a way so as to design a problem as if it were a quasi-static problem. The analytical results for a quasi-static problem are known and can be compared to the numerical results, thereby, verifying the model on this platform for this specific problem.

Boundary Conditions:

- **Laterally constrained:**

- All faces, displacements in 1 and 3 directions, $u_1 = u_3 = 0$
- Bottom face, $u_2 = 0$
- Top face, $u_2 = LT$ (where, L is the height of the cube = $1m$ and T is the total time of run)

- **Laterally free**

- Left face, $u_1 = 0$
- Back face, $u_3 = 0$
- Bottom face, $u_2 = 0$
- Top face, $u_2 = LT$ (where, L is the height of the cube = $1m$ and T is the total time of run)

Initial Conditions:

- **Laterally constrained:**

- Displacements, $u_1 = u_2 = u_3 = 0$
- Velocities, $v_2(X) = X(x_2)$ (where, X is the position vector and x_2 is the coordinate in ‘y’ or ‘2’ direction)

- **Laterally free:**

- Displacements, $u_1 = u_2 = u_3 = 0$
- Velocities, $v_1 = \Upsilon.x_1, v_2 = x_2, v_3 = \Upsilon.x_3$

where, $\Upsilon = \frac{-C_{12}}{C_{11}+C_{12}}$

3.4.4.1 Verifying the 3D Elastic response

It is expected that the average-stress versus average-strain curve has a slope equal to Young’s modulus in Laterally Free case, whereas, slope should be equal to C_{11} (component of the Elasticity Tensor) in Laterally Constrained case. In Laterally Free case, Poisson’s effect is considered and a change in cross-section of the specimen is allowed. However, in Laterally Constrained case, no change in cross-section of the specimen is allowed.

The results are shown in Figure 3.10. As clearly seen in the figure, the slope of the laterally constrained case corresponds to C_{11} , whereas, the slope of the laterally free case is equal to the Young’s modulus.

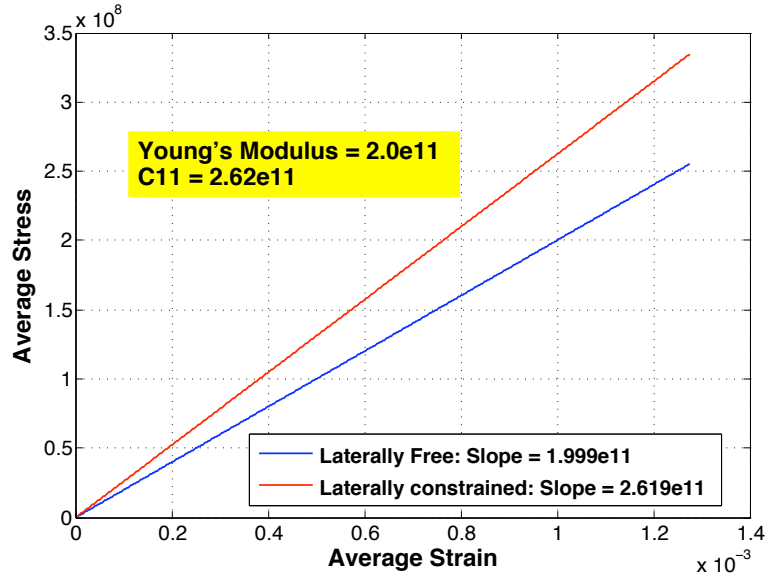


Figure 3.10 – Elasticity verification – Tension. *Units: stress (N/m^2)*

3.4.4.2 Verifying the 3D Elasto-plastic response

The elasto-plasticity verification in Tension is a 2-step process for a dynamic setting. This is because the initial conditions for the velocity change at the onset of plasticity compared to what they would otherwise be in a purely elastic case. The 1st step of verifying elasticity is already done above.

The initial conditions on velocity for plasticity verification are:

- $v_1(t = 0) = \Upsilon x_1(1 - \dot{\varepsilon}_p(2, 2)) + \dot{\varepsilon}_p(2, 2)x_1$
- $v_2(t = 0) = x_2$
- $v_3(t = 0) = \Upsilon x_3(1 - \dot{\varepsilon}_p(2, 2)) + \dot{\varepsilon}_p(2, 2)x_3$

where, $\dot{\varepsilon}^p$ is plastic strain rate, x_i is the coordinate value in i^{th} direction, and

$$\Upsilon = \frac{-C_{12}}{C_{11} + C_{12}}$$

The values of plastic strain rate ($\dot{\epsilon}^p$) and displacements (u) are saved a couple of increments before the yield point in a usual elasto-plastic simulation, which are then used to set up new initial conditions to verify plasticity only.

Figures 3.11 and 3.12 show comparison between analytical and numerical results for the J2 plasticity and the Drucker-Prager plasticity cases respectively. As seen in the figures the numerical and analytical results match.

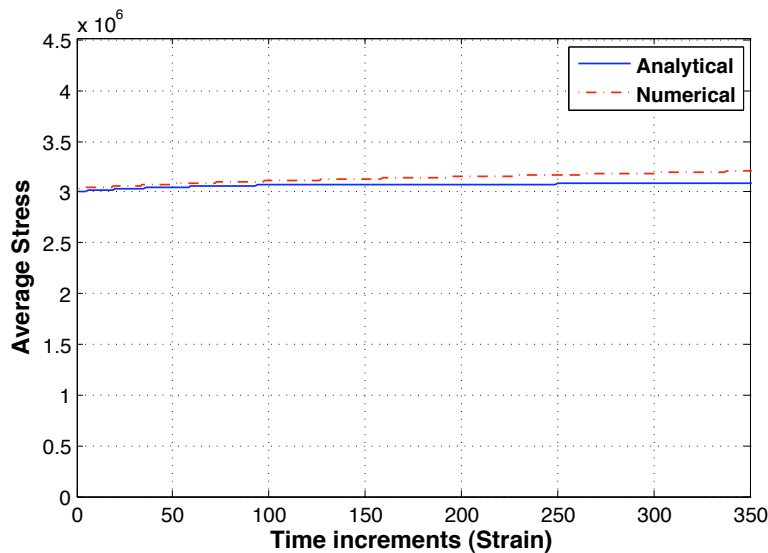


Figure 3.11 – Plasticity verification (J2). Units: stress (N/m^2)

3.4.4.3 Verifying the 3D response for coupled Elasto-plasticity and damage

In this case also, the values of plastic strain rate ($\dot{\epsilon}^p$) and displacements (u) are saved a couple of increments before the yield point in a usual elasto-plastic simulation, which are then used to set up new initial conditions to

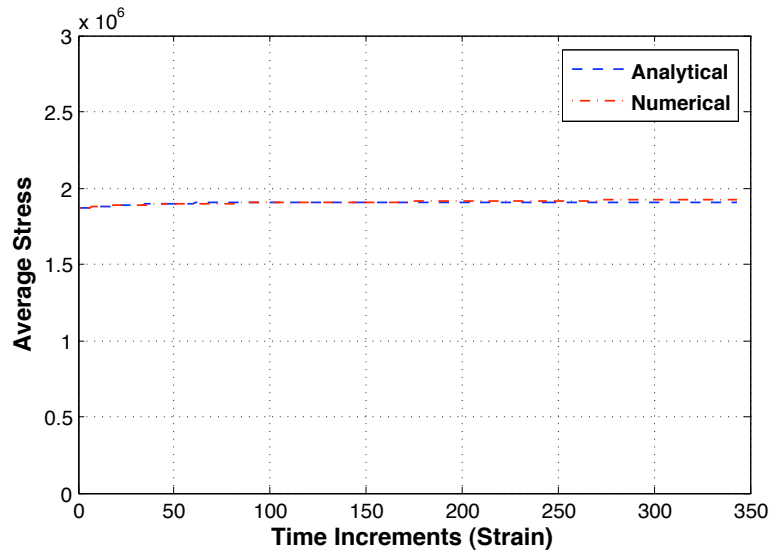


Figure 3.12 – Plasticity verification (Drucker-Prager). *Units: stress (N/m^2)*

verify plasticity only. Further, as mentioned before the void-volume growth is controlled by a constant value after each increment.

Figures 3.13 and 3.14 show comparison between analytical and numerical results for the J2 plasticity and the Drucker-Prager plasticity cases with void-volume fraction contribution respectively. The material softening is observed and the numerical and analytical results match.

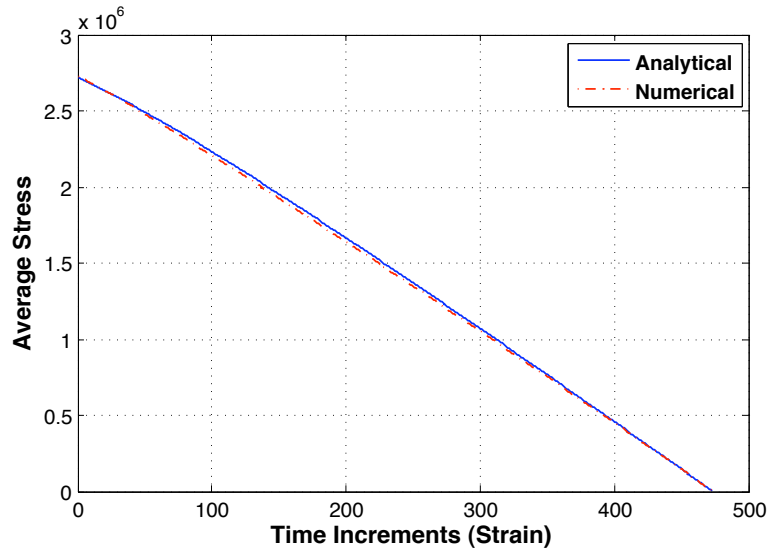


Figure 3.13 – Material softening with damage (J2). *Units: stress (N/m^2)*

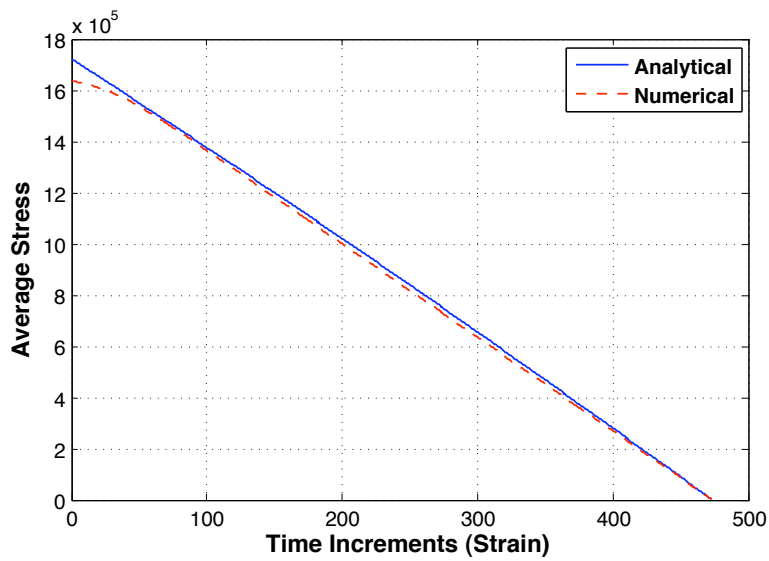


Figure 3.14 – Material softening with damage (Drucker-Prager). *Units: stress (N/m^2)*

Chapter 4

Uniaxial Compression Problem

4.1 Introduction

The dynamic ductile damage model was verified and validated in the last chapter. We can now use it to solve a full-scale coupled pure uni-axial compression problem with both the governing equations (balance of linear momentum and damage evolution equations) active. The damage as mentioned earlier is controlled by Plasticity or in other words, the damage shall propagate or evolve at the onset of Plasticity. Figure 4.1 shows the setup for a uniaxial compression test.

Individual cases of unconstrained and completely constrained setups with respect to applied boundary conditions and loading conditions are discussed in detail in the following sections. However, in both the cases it is assumed

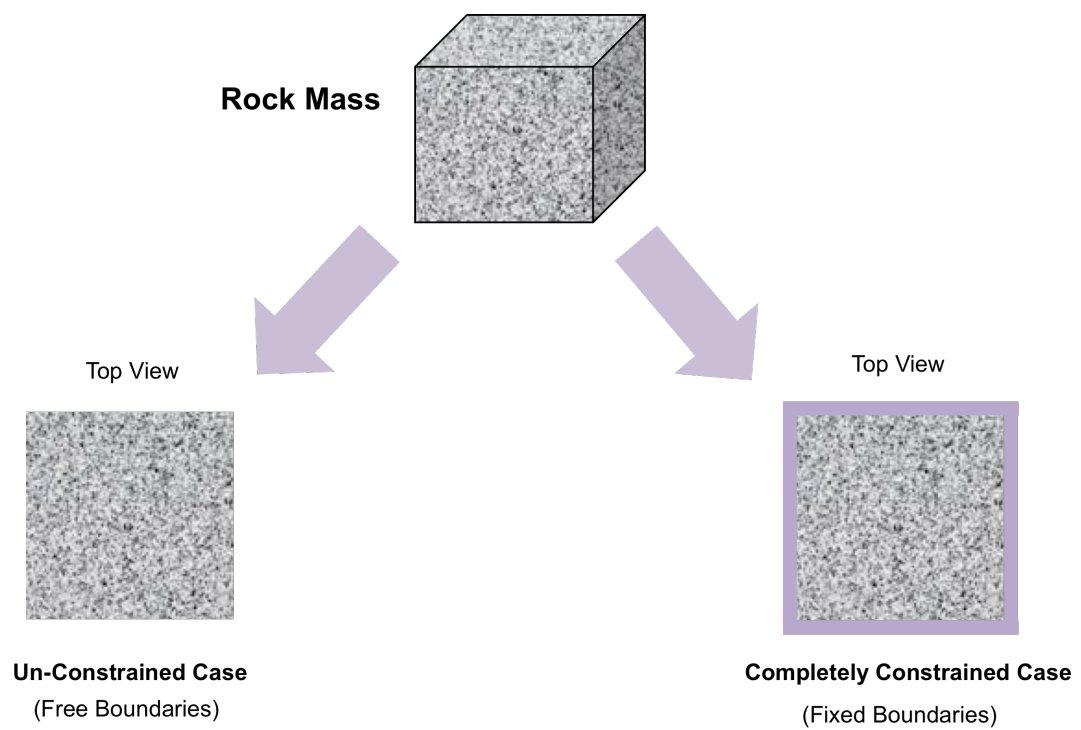


Figure 4.1 – Uniaxial Compression Setup

that there is some initial uniform distribution of voids, which we represent as void-volume fraction (number of voids per unit control volume) in our numerical model. For the problem under consideration, we start with 10% initial void-volume fraction. The problem is simulated with both the local and non-local schemes for unconstrained as well as completely constrained cases respectively.

The following list shows the materials properties for the specimen considered:

- Material Type – Rock (sandstone)
- Density – 2500kgm^{-3}
- Young's Modulus – $4.3 \times 10^9\text{Nm}^{-2}$
- Poisson's Ratio – 0.25
- Yield Strength – $14 \times 10^6\text{Nm}^{-2}$
- Friction Coefficient – 0.6
- Dilatancy Coefficient – 0.5

4.2 Unconstrained Case

Figure 4.2 gives the details of the loading and boundary conditions for the unconstrained compression case. As is clear from the figure, the boundaries are free complementing the unconstrained setup with a fixed base. The loading is uniform over the top face.

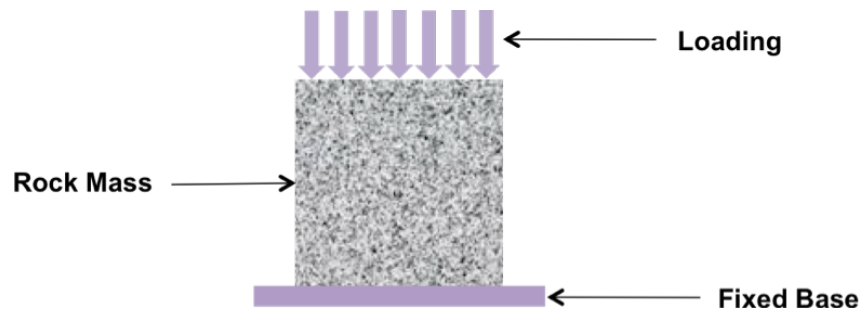


Figure 4.2 – Uniaxial Unconstrained Compression Setup

The simulations for the unconstrained case were carried out for the local as well as the non-local schemes and the results for the same followed by their comparison is presented below.

4.2.1 Unconstrained Local

Figure 4.3 shows the results for the unconstrained local scheme. We chose two mesh sizes:

- 40 by 40 by 1 elements
- 50 by 50 by 1 elements

The plot compares the average stress versus average strain curves for the two mesh sizes mentioned above. The simulations for both the mesh sizes were allowed to run up to 100% void-volume fraction. As is clear from the figure, the curves look converged. A close look at the curves for both mesh sizes shows intermittent peaks and oscillations. This is due to wave reflections from the boundaries of the material specimen. The other results that follow in this

thesis show similar peaks and oscillations for the same reason as mentioned above.

The convergence can be attributed to the uniform loading of the rock mass and the rate-dependent scheme employed. In order to explain it further, we consider the local-1D problem the results for which were presented in an earlier chapter 2, sub-subsection 2.1.6.2, figures 2.8 and 2.9 respectively. These figures represent the simulations that were carried out for the two material cases, one with low rate-sensitivity and the other with high rate-sensitivity. The field plots of plastic strain for the two cases were plotted at the same physical time for three different mesh refinements. A comparison clearly showed the stabilizing effect of the rate-sensitivity. The higher value of rate-sensitivity ensured better convergence. It is also important to mention here that even a very low value of rate-sensitivity has some stabilizing effect compared to a completely rate-independent scheme, where the strains shoot up with mesh refinement.

4.2.2 Unconstrained Non-Local

We considered three mesh sizes for the non-local case:

- 40 by 40 by 1 elements
- 50 by 50 by 1 elements
- 60 by 60 by 1 elements

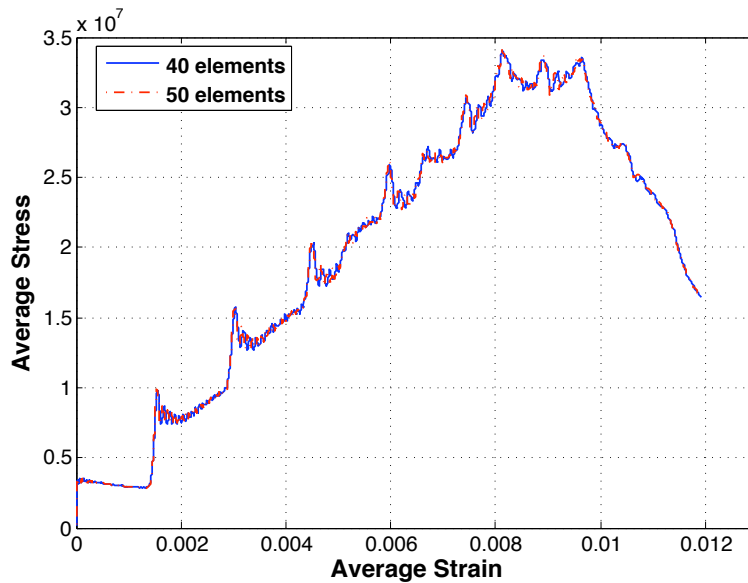


Figure 4.3 – Av. Stress vs Av. Strain (LOCAL). *Units: stress (N/m^2)*

Figure 4.4 shows the results for the unconstrained non-local scheme. Here also, the simulations for all the mesh sizes were allowed to run up to 100% void-volume fraction. The plot compares the average stress versus average strain curves for the three mesh sizes mentioned above. As expected the curves look converged. This is owing to the stable nature of the non-local scheme as has been shown earlier for many different cases.

4.2.3 Unconstrained Local vs Non-Local

Now we can draw a comparison between the local and the non-local schemes for the unconstrained compression. Figure 4.5 shows the comparative plot of average stress versus average strain curves for the local and non-local schemes

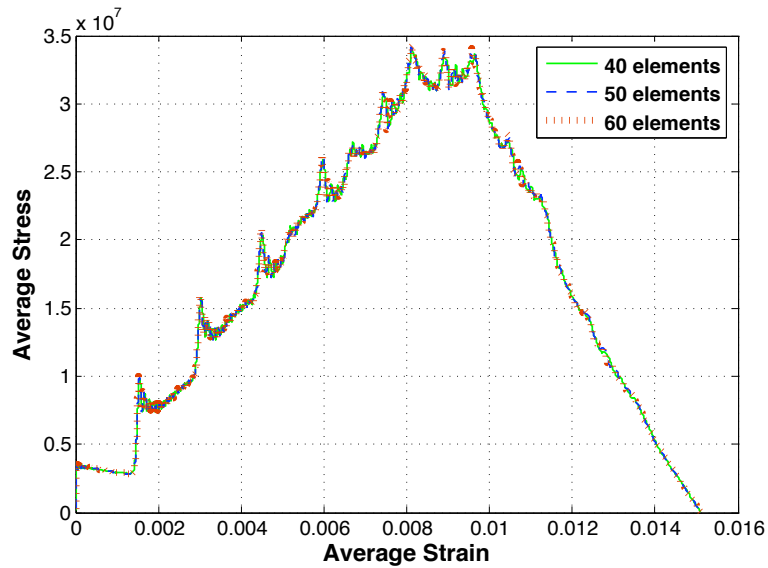


Figure 4.4 – Av. Stress vs Av. Strain (NON-LOCAL). *Units: stress (N/m²)*

for a common mesh size. We can conclude that owing to a more stable nature of the non-local scheme, the failure as expected is delayed in terms of failure strain compared to that of the local scheme.

4.3 Completely Constrained Case

The details of the loading and the boundary conditions for the completely constrained case are shown in Figure 4.6. The lateral constraints are provided in the form of rigid displacement control. Visually we can refer to lateral constraints as the lateral pressure that the rock mass experiences under the conditions of High Pressure. The simulations for the constrained case were carried out for the local as well as the non-local schemes and the results for

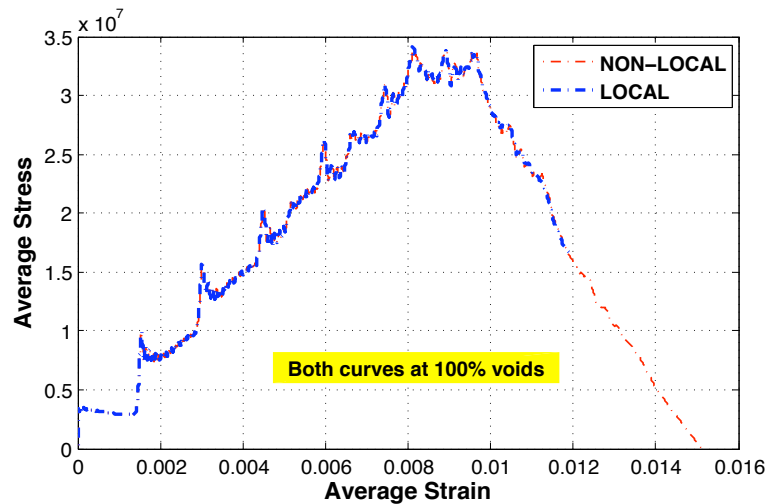


Figure 4.5 – Av. Stress vs Av. Strain (LOCAL vs NON-LOCAL). *Units: stress (N/m^2)*

the same followed by their comparison is presented below.

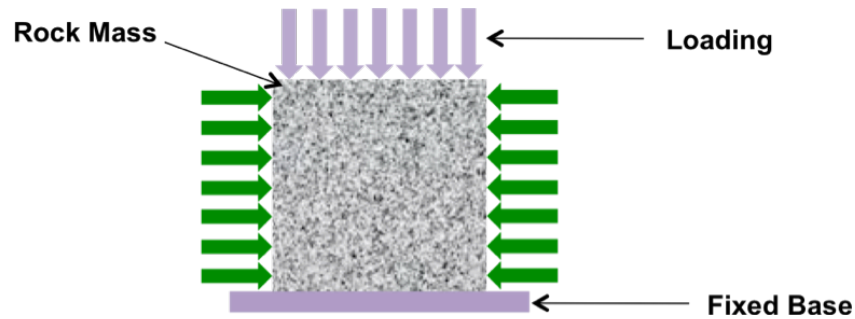


Figure 4.6 – Uniaxial constrained compression setup

4.3.1 Completely Constrained Local

Figure 4.7 shows the results for the constrained local scheme. We chose two mesh sizes:

- 40 by 40 by 1 elements
- 80 by 80 by 1 elements

The plot compares the average stress versus average strain curves for the two mesh sizes mentioned above. The simulations for both the mesh sizes were allowed to run up to 100% void-volume fraction. As is clear from the figure, the curves look converged.

The argument for the convergence in the local case that was presented earlier for the unconstrained local case stands here as well.

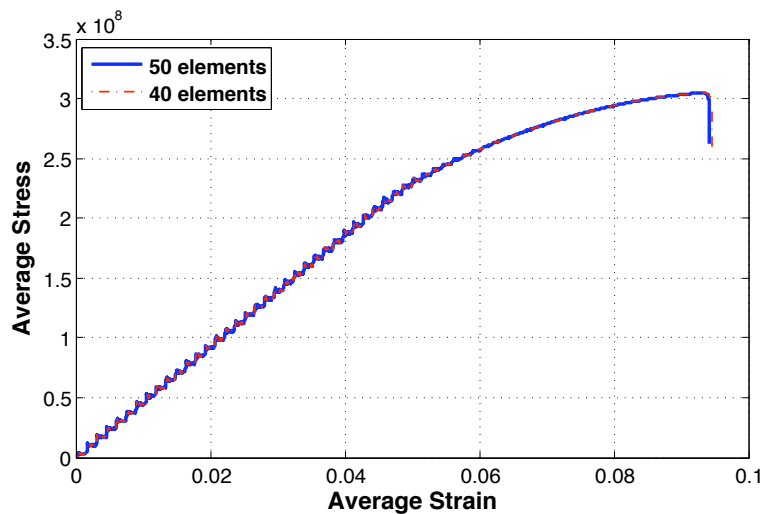


Figure 4.7 – Av. Stress vs Av. Strain (LOCAL). *Units: stress (N/m^2)*

4.3.2 Completely Constrained Non-Local

We considered the following two mesh sizes for the non-local case:

- 40 by 40 by 1 elements

- 50 by 50 by 1 elements

Figure 4.8 shows the results for the constrained non-local scheme. The simulations for both the mesh sizes were allowed to run up to 100% void-volume fraction. The plot compares the average stress versus average strain curves for the two mesh sizes mentioned above. As expected the curves look converged. This is owing to the stable nature of the non-local scheme as has been mentioned many time before.

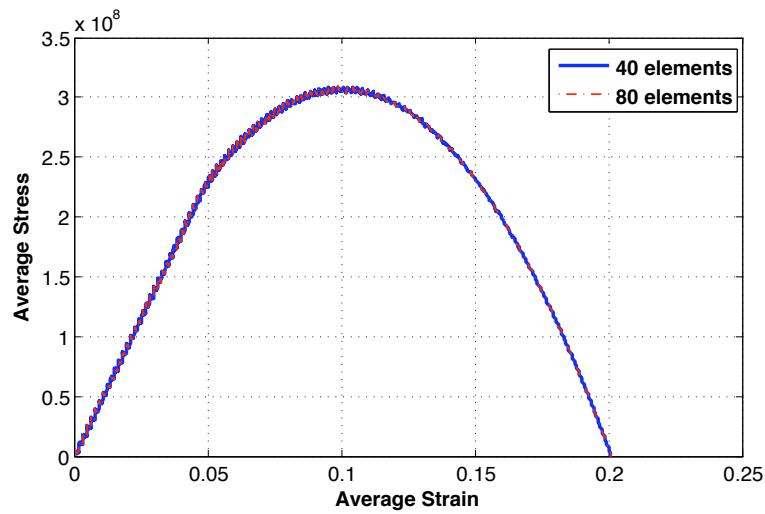


Figure 4.8 – Av. Stress vs Av. Strain (NON-LOCAL). *Units: stress (N/m^2)*

4.3.3 Completely Constrained Local vs Non-Local

Figure 4.9 shows the comparative plot of average stress versus average strain curves for the local and non-local schemes for a common mesh size. Owing to the more stable nature of the non-local scheme, the failure as expected is

delayed in terms of failure strain compared to that of the local scheme. In particular for the case of completely constrained rock mass, the non-local failure strain is almost double the local failure strain.

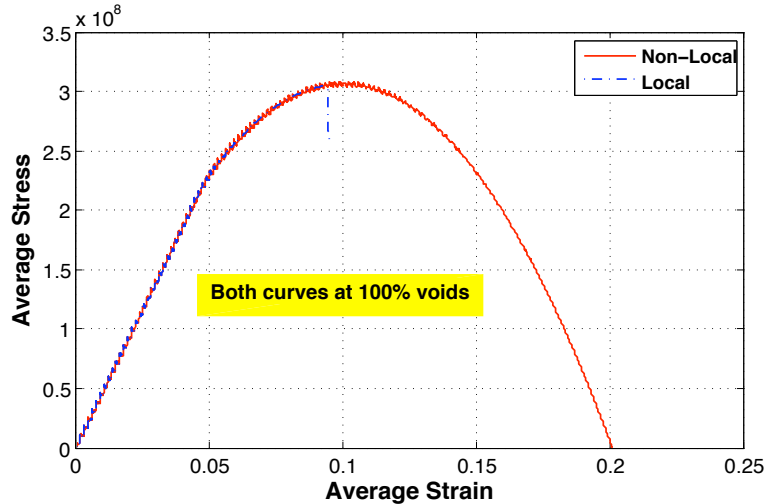


Figure 4.9 – Av. Stress vs Av. Strain (LOCAL vs NON-LOCAL). *Units: stress (N/m^2)*

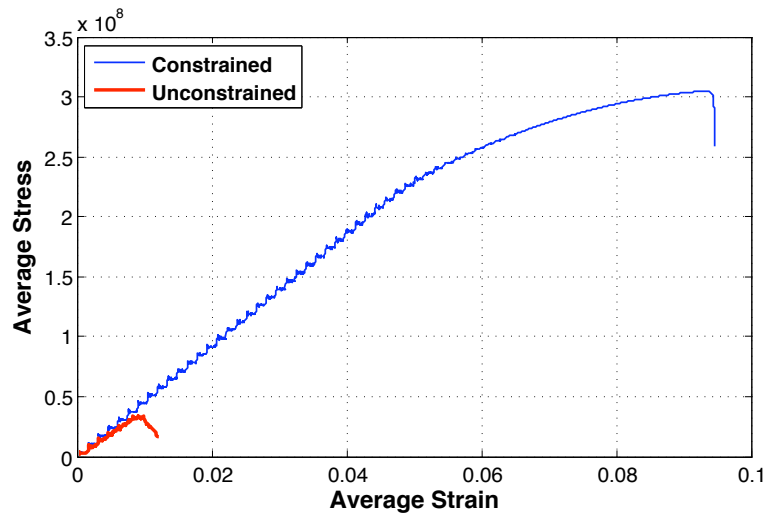
Now, in the following sub-section we may look at the relative comparison between the unconstrained and the completely constrained cases respectively.

4.4 Unconstrained versus Completely Constrained Compression

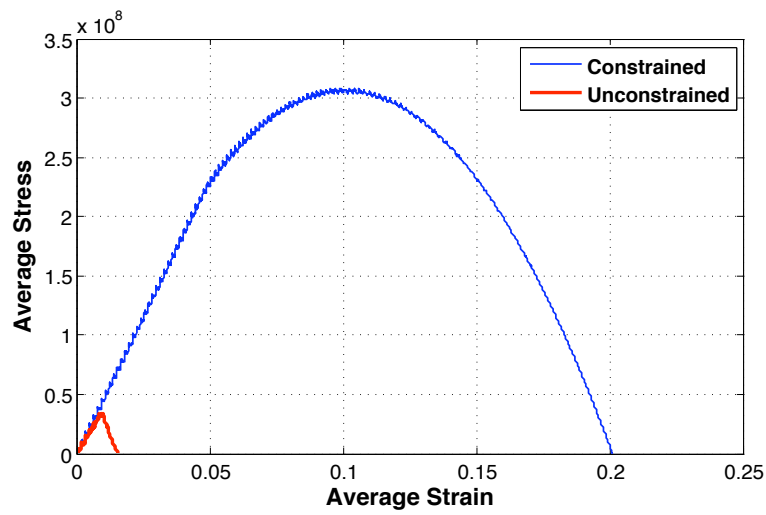
Figure 4.10 shows the comparison between the unconstrained and the completely constrained cases for both local and non-local schemes respectively. The comparison is made for a single mesh size for both the cases.

The figure gives us a clear indication of what it means dealing with the conditions of High Pressure. From the above curves, we are looking at maximum vertical pressure of around $45,000psi$. There is an exorbitant difference in the failure strains between the constrained and the unconstrained cases. The difference in particular is more in the non-local comparison.

In other words Figure 4.10 is an indication of the difficulty in drilling deep inside the earth's crust where High pressures increase the failure strains by huge margins.



(a)



(b)

Figure 4.10 – Av. Constrained vs Unconstrained; (a) LOCAL, (b) NON-LOCAL. Units: stress (N/m²)

Chapter 5

The Dynamic Indentation Problem

5.1 Introduction

In this chapter, we shall focus on simulating an idealized drilling process, which may be numerically represented as a dynamic indentation problem. Of course dynamic indentation of a rock mass will be considered. It may be noted that the coupling mechanism shall remain in place and active. The void-volume fraction will be driven by plasticity and Drucker-Prager plasticity model will be employed as discussed earlier.

Modeling an indenter is complimentary to mechanical evacuation of various rock types using drill cutters. Usually, rock cutters act vertically as well as

horizontally on a rock face thereby inducing normal and shearing stresses. In an idealized setting, the indenter may be assumed to be acting in normal direction only. Figure 5.1 gives a schematic representation of a rock body under the action of an idealized indenter.

The indentation in the numerical model may be provided in the form of displacement at the otherwise location or line of action of an indenter. The goal will be to reproduce typical reaction force- displacement curves as well as verify to what extent the model is able to reproduce the three zones of crushed material, cracked zone, and intact elastic zone observed in experiments (Abd Al-Jalil, Y.Q 2006).

5.2 Indenter Modeling - Set up

Figure 5.1 shows a rock body under the action of an idealized indenter.

The typical mesh structures used are shown in Figure 5.2. Here it may be noticed that refinement occurs only in the upper layers since it is in the top region only where most of the activity takes place. It also helps to improve computational efficiency. A sharp but smooth Gaussian is used as a displacement profile to realistically correlate it to an indenter on rock body. The profile seen in Figure 5.3 is plotted at the end of the simulation from output to verify correct application of boundary conditions.

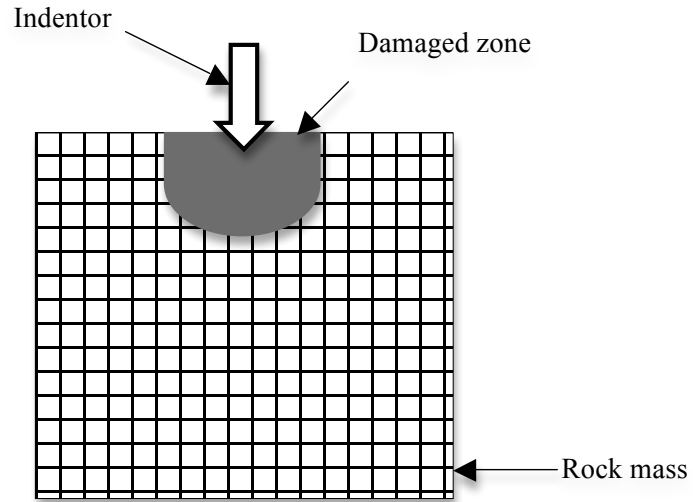


Figure 5.1 – Idealized Indenter showing rock body and damaged zone

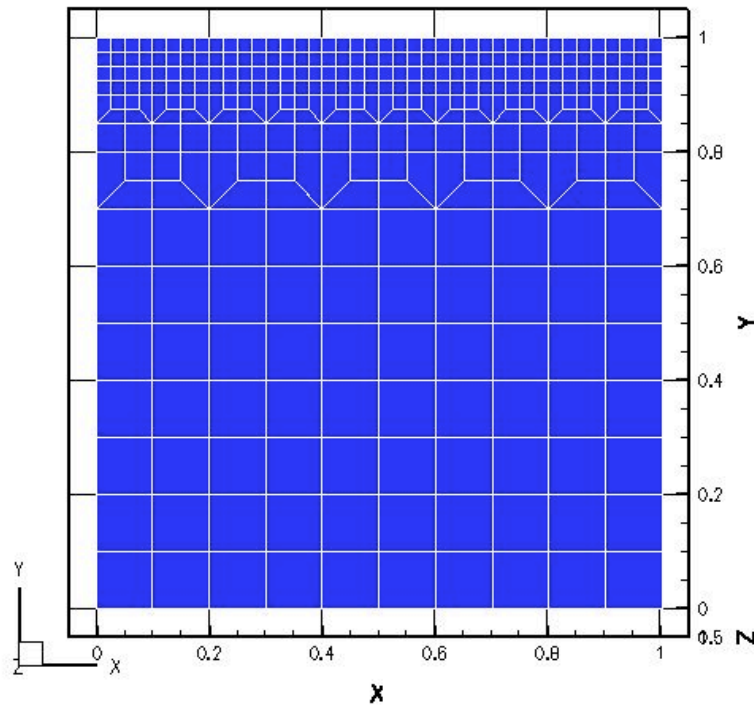


Figure 5.2 – Typical Mesh Refinement

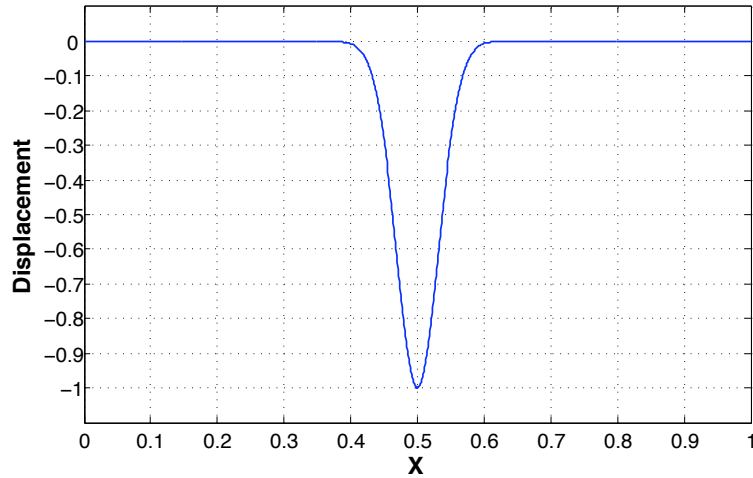


Figure 5.3 – Displacement profile in the form of a Gaussian. *Units: distance (m), displacement (m)*

5.3 Local Case

Numerically, keeping only the source term in the void-volume fraction equation simulates the local case. Therefore, the void-volume fraction equation looks like:

$$\dot{\varphi} = s$$

The results for the local case are presented now. Simulations were carried out for different mesh structures. The main idea is to check convergence. If the results corresponding to different mesh sizes match in the local case then there is no need to entertain non-local case at all.

Figure 5.4 shows the plot between average stress versus average strain corresponding to the selected mesh structures. It can be immediately confirmed

that the curves representing respective mesh sizes do not converge.

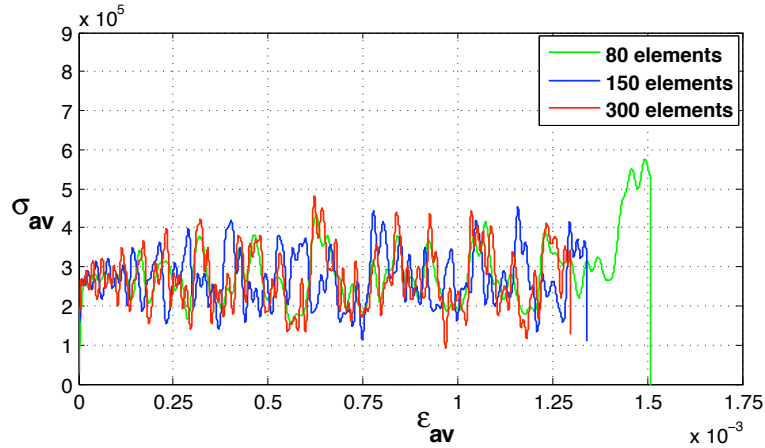


Figure 5.4 – Average Stress versus Average Strain for two mesh sizes. *Units: stress (N/m^2)*

Let us look at the field plots of void-volume fraction at the end of the simulations for the two mesh sizes respectively. Figure 5.5 shows two field plots for meshes 150 elements and 300 elements respectively. Here again, the plots do not converge. Also, for the finer mesh, the distribution of the void-volume fraction is highly localized at two locations, which is contrary to experimental observations (Abd Al-Jalil, Y.Q.,” The Mechanics of Indentation of Rock – A Critical Review”, The 41st Symposium of USRMS, Golden, Colorado, June 17-21, 2006).

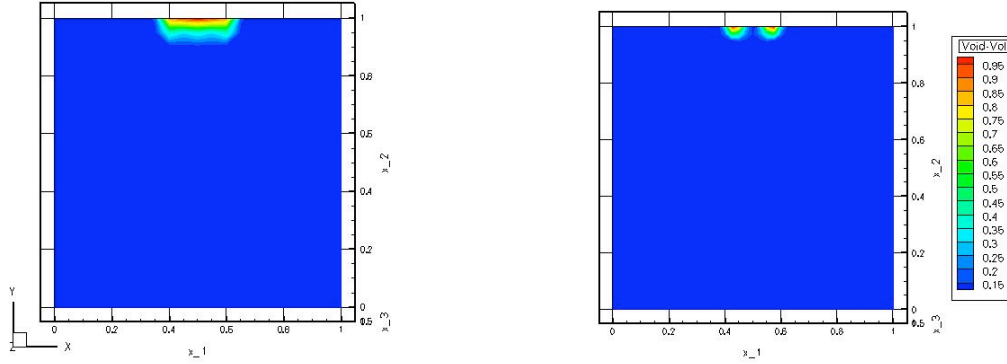


Figure 5.5 – Field plots for void-volume fraction; (a) 150 elements, (b) 300 elements. *Units: distance (m)*

5.4 Non-Local Case

As in the local case, the simulations were carried out for different mesh sizes respectively. However, one of the most critical factors for the success of the non-local case and its advantage over the local behavior is the requirement of a spatially uniform damage driving variable in the diffusion term of the damage evolution equation. The diffusion coefficient is dependent on the value damage driving variable w . In other words, the diffusion coefficient field has to remain non-zero in the body without sharp changes. This is especially important at the damaged/undamaged zone boundary.

The choice of a spatially uniform w is made as follows:

Let j_{elem} represent element number and $w_{j_{elem}}$ damage driving variable for that element. Then for a particular time increment N , we have:

$$w = \max(w_{jelem})$$

We take the maximum value of w of all the elements in a single time increment to calculate the diffusion coefficient for that increment. Therefore, the diffusion coefficient increases with the increase in the maximum w used. The constitutive assumption that gave good post-localization behavior also implies that the diffusion coefficient increases in proportion to the spatially averaged damage driving variable. The initial displacement in the top layer of nodes is provided in the form of a sharp gaussian to simulate the indentation process. This gaussian creates sharp gradients between the loaded and unloaded elements or in other words at the damaged/undamaged zone. So, no matter how large the diffusion coefficient is, the solution still blows up and the output is more like a local output rendering the non-local concept ineffective. This is one of the major findings of our research that for a sharp displacement profile like a gaussian, it is imperative that the diffusion coefficient remain non-zero in the body. However, for the source term, it is the individual value of w for each gauss point of each element that is considered.

Figure 5.6 shows the plots of average stress versus average strain for the mesh sizes respectively. It may be noticed that the results are converged for the finer mesh sizes.

Now, let us look at the field plots of void-volume fraction for mesh sizes 150 and 300 elements respectively. Figure 5.7 shows the field plots of void-volume

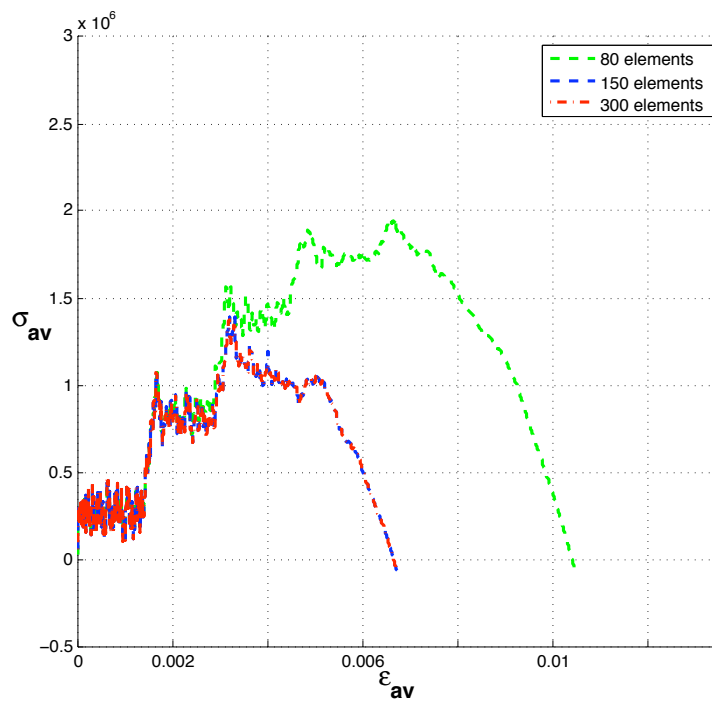


Figure 5.6 – Average Stress versus Average Strain for different mesh sizes.
Units: stress (N/m²)

fraction for the above converged mesh sizes (150 and 300 elements respectively) at the same physical time at failure. It is clear that the results are converged, though the field plot for the finer mesh looks smoother understandably.

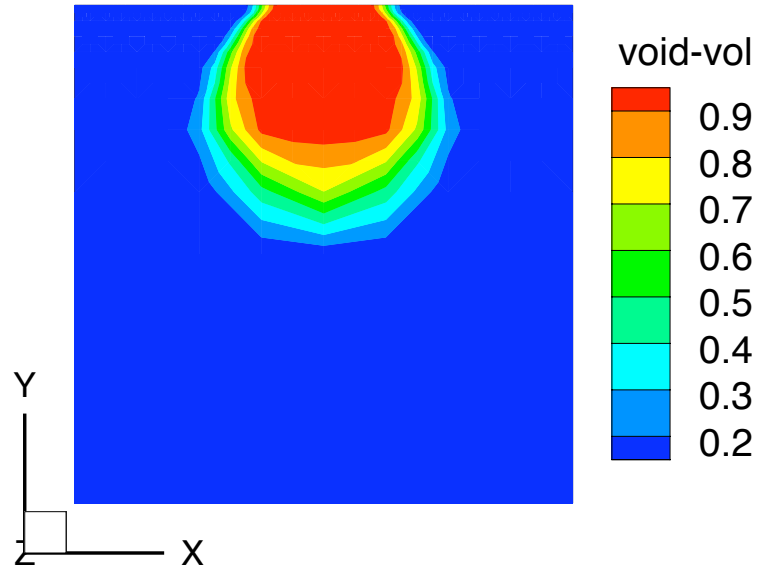
The field plots of stress in direction 2-2 also look converged as seen in Figure 5.8. These plots correspond to the maximum stress values attained at the onset of softening, i.e. at around the strain of 0.003 in Figure 5.6

5.5 Temperature Effects

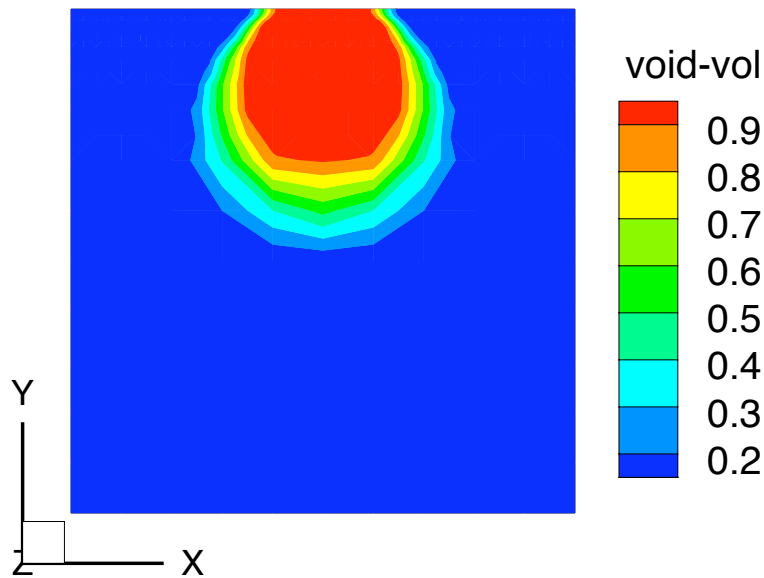
Now that the non-local model is established as a pressure dependent model capable of handling extreme pressures, such pressures that exist deep inside the earth's crust at $10,000ft$ and beyond, we shall add another physical quantity to the model, which is Temperature.

Temperature is an important factor as far as ultra deep drilling is concerned with temperatures ranging from $150^{\circ}C$ to $250^{\circ}C$ at such depths. The rise in temperature has a direct effect on the flow stress of a material. We shall make use of the following two laws to understand the effect of temperature on the material behavior.

- Exponential Law
- Power Law



(a)



(b)

Figure 5.7 – Field plots for void-volume fraction; (a) 150 elements, (b) 300 elements. *Units: distance (m)*

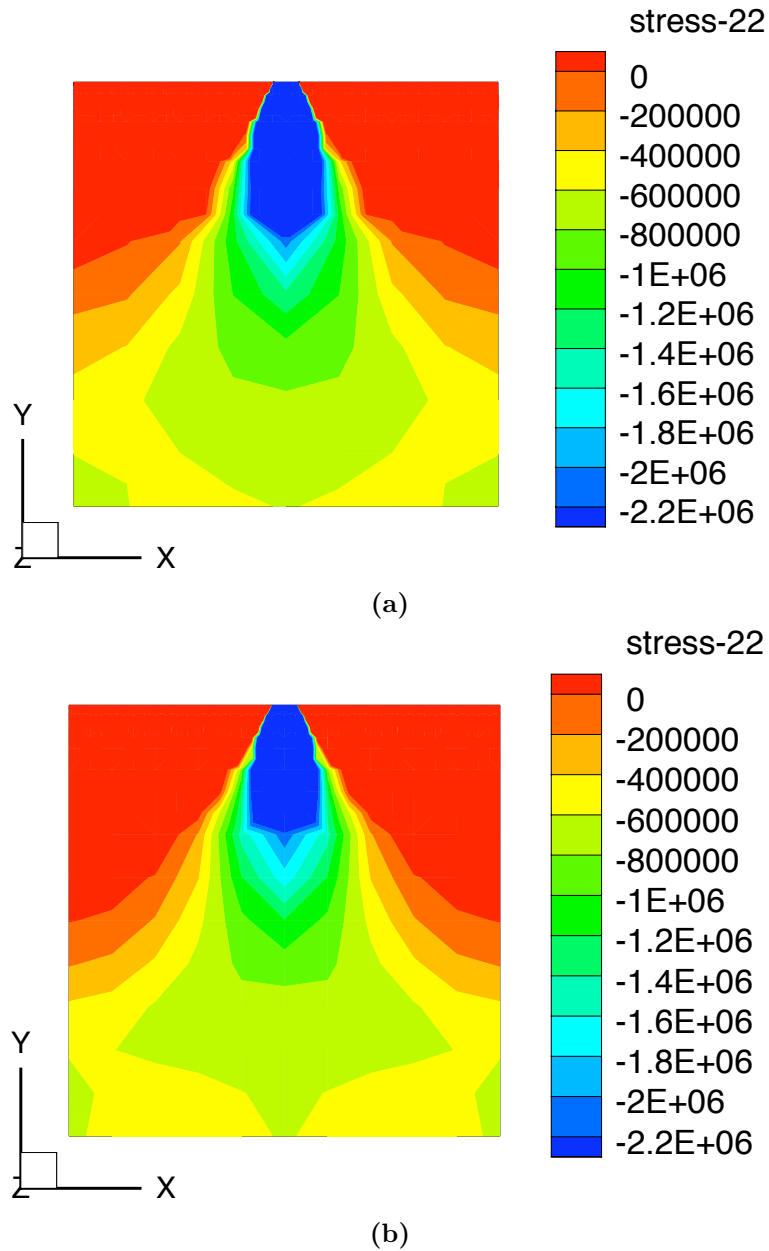


Figure 5.8 – Field plots for stress; (a) 150 elements, (b) 300 elements. *Units: stress (N/m^2), distance (m)*

5.5.1 Exponential Law

The yield equation, which formerly was:

$$\tau = \hat{\tau}(1 - \varphi)$$

now becomes (Mainprice, D., Paterson, M. 2005);

$$\tau = \hat{\tau}(1 - \varphi)e^{(-a(\Theta - \Theta_0))}$$

where, $\hat{\tau}$ is flow stress, a is material parameter, Θ is temperature and Θ_0 is standard temperature at ground level.

Figure 5.10 shows the comparison of the two curves of average stress versus average strain corresponding to two temperatures $100^\circ C$ and $200^\circ C$ respectively. The simulations for the two temperature conditions were carried on the same mesh size. The values of constants were chosen as:

- $a = 2.23 \times 10^{-3}$
- $\Theta_0 = 300K$

The figure suggests that failure takes place at a lower strain for a particular material at higher temperature. However, increasing the value of the material parameter ' a ' to 3.95×10^{-3} further decreases the failure strain for both temperatures respectively as can be observed in Figure 5.10.

If there are two materials with different values of ' a ', we may compare them

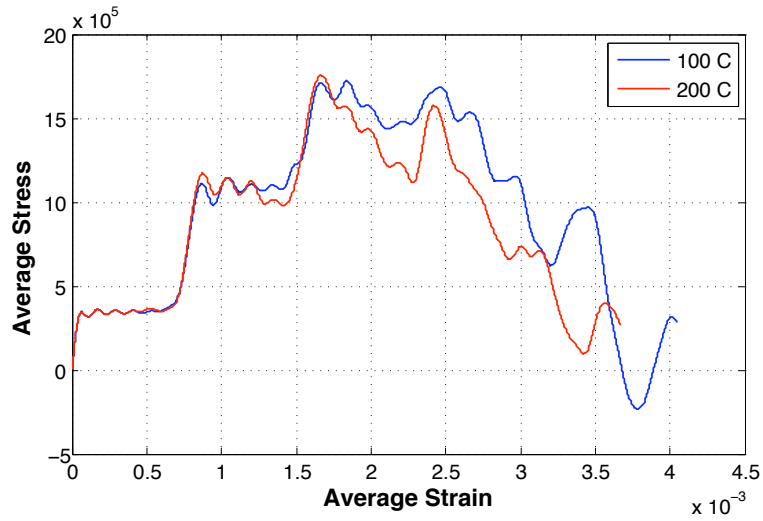


Figure 5.9 – Comparison: at two different temperatures. *Units: stress (N/m^2)*

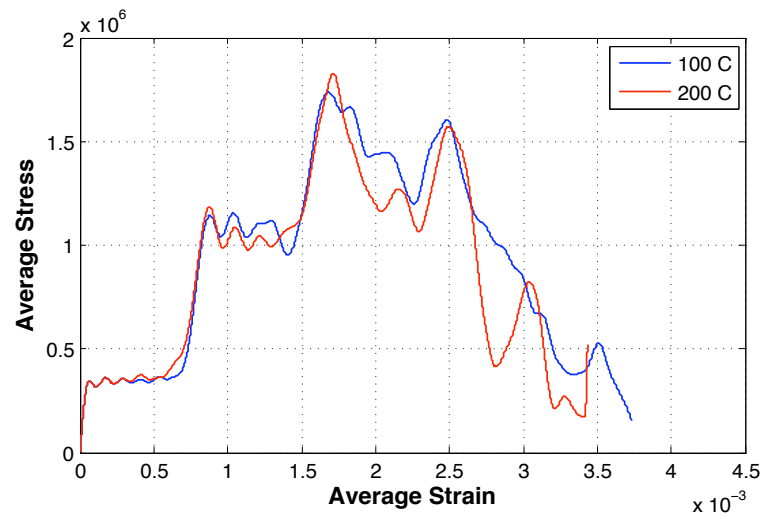


Figure 5.10 – Comparison: at two different temperatures with higher value of 'a'. *Units: stress (N/m^2)*

at the same temperature. Figure 5.11 shows a plot of average stress versus average strain at 100°C for two materials with different ‘ a ’. It may be concluded that materials with higher value of ‘ a ’ are more responsive to temperature rise than the ones with lower value of ‘ a ’.

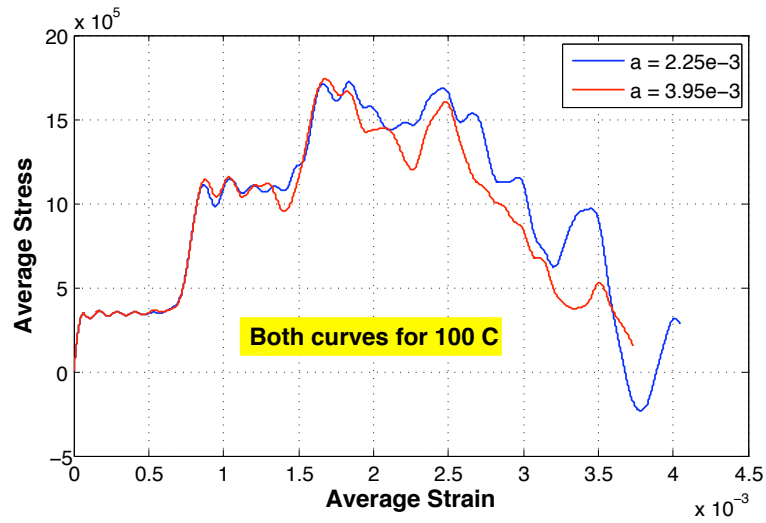


Figure 5.11 – Comparison: different ‘ a ’ at same temperature. *Units: stress (N/m^2)*

5.5.2 Power Law

The yield equation in case of the power law becomes (Fung, Y., Tong, P. 2001):

$$\tau = \hat{\tau}(1 - \varphi) \left(\frac{\Theta}{\Theta_0} \right)^{-g_t}$$

where, g_t is material parameter.

Figure 5.12 shows the comparison of the two curves of average stress versus

average strain corresponding to two temperatures 100°C and 200°C respectively. The simulations for the two temperature conditions were carried on the same mesh size. The values of constants were chosen as:

- $g_t = 0.75$
- $\Theta_0 = 300\text{K}$

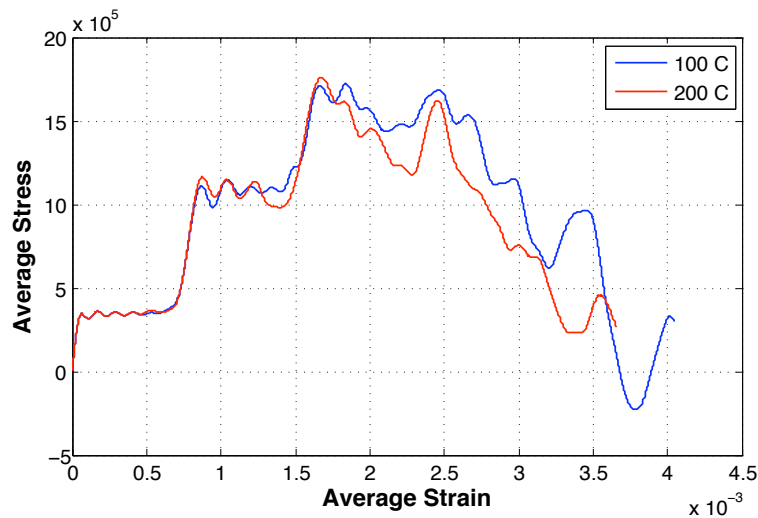


Figure 5.12 – Comparison: at two different temperatures. *Units: stress (N/m^2)*

The figure in case of the power law as in case of the exponential law suggests that failure takes place at a lower strain for a particular material at higher temperature. However, increasing the value of the material parameter ‘ g_t ’ to 1.32 further decreases the failure strain for both temperatures respectively as can be observed in Figure 5.13.

If there are two materials with different values of ‘ g_t ’, we may compare them at the same temperature as we did for the exponential law. Figure 5.14 shows

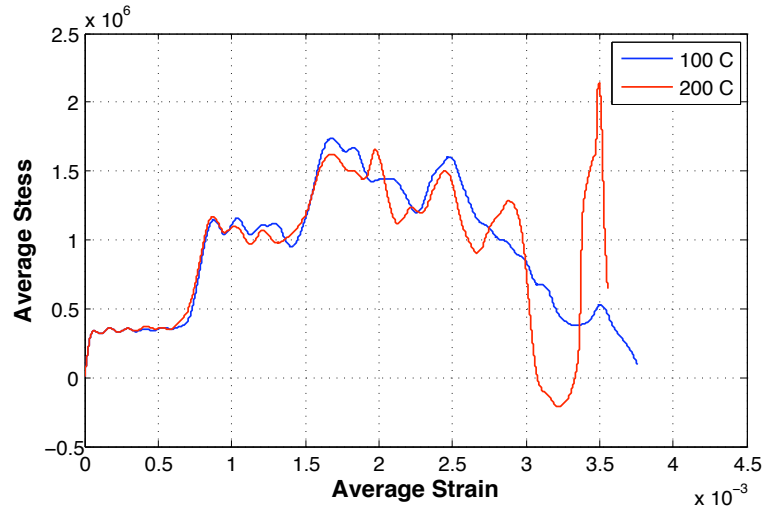


Figure 5.13 – Comparison: at two different temperatures with higher value of ‘ g ’. Units: stress (N/m^2)

a plot of average stress versus average strain at 100°C for two materials with different ‘ g_t ’. It may be concluded that materials with higher value of ‘ g_t ’ are more responsive to temperature rise than the ones with lower value of ‘ g_t ’.

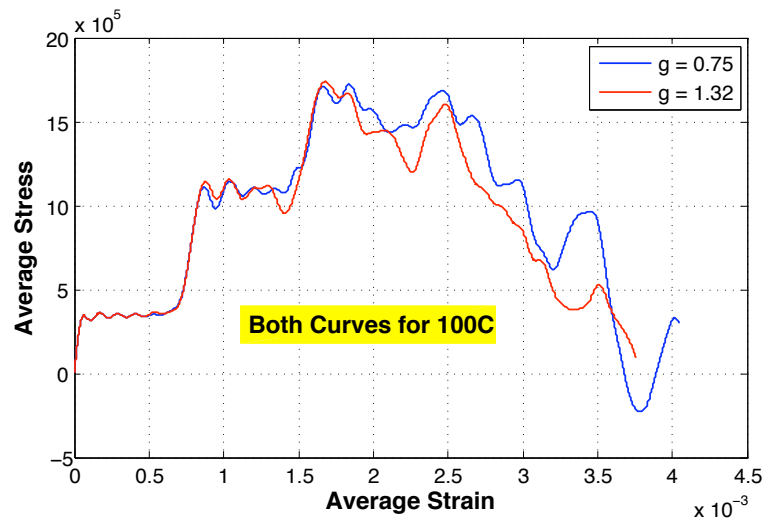


Figure 5.14 – Comparison: different ‘ g ’ at same temperature. *Units: stress (N/m^2)*

Chapter 6

Conclusion

The aim of this research was to develop a numerical tool that can realistically model the behavior of rocks and their failure criteria under the extreme conditions of High Pressure and High Temperature (HPHT).

As mentioned before, the behavior of rocks under HPHT is very different than under the normal conditions of pressure and temperature. Due to confinement the fragments can stay together and flow like a continuum thus demonstrating ductile behavior.

The conventional models and theories of material behavior have no intrinsic material length scale, thereby, predicting deformation bands of zero thickness, which is physically incorrect. In this research, the more suited and stable behavior of non-local modeling was proven to score over conventional theories and models. In particular the introduction of the concept of void-volume

fraction is an important contribution, which is physically more justifiable than just considering voids only and some damage parameter.

The 3D non-local numerical model was applied to an idealized rock-cutting problem, which in the present case is the dynamic indentation of a rock mass. The model demonstrated qualitatively correct behavior of the rock body under an indentation. The indentation bulb profile is similar to experimental observations (Abd Al-Jalil 2006). However, it is important to point out that a spatially uniform damage driving variable in the diffusion term is required. In other words, the diffusion coefficient field has to remain non-zero in the body without sharp changes. This is especially important at the damaged/undamaged zone boundary to avoid sharp gradients, which make the problem unstable. The uniform diffusion coefficient is dependent on the value damage driving variable w . We take the maximum value of w of all the gauss point values of all the elements in a single time increment to calculate the diffusion coefficient for that increment. Therefore, the diffusion coefficient increases with the increase in the maximum w used. The constitutive assumption that gave good post-localization behavior also implies that the diffusion coefficient increases in proportion to the spatially averaged damage driving variable. This implies that work needs to be done in this regard to identify a variable with a physically rigorous corresponding constitutive theory.

The other aspect that needs to be addressed is the use of material constants. Experimental data is required to get the correct values of certain material parameters used. For example, the constant B , which is used in the diffusion

term of the damage evolution equation, needs to be quantified correctly for a specific material. The Ultra Deep Drilling Simulator (UDS) kind of experimental setups should definitely help.

Also, in the present research the rock cutter is assumed to act in normal direction. Realistic modeling, however, requires accomodation of contact. This is something to look at in the future.

Bibliography

- [1] Drucker, D. C. and Prager, W. 1952, "Soil mechanics and plastic analysis for limit design." Quarterly of Applied Mathematics, vol. 10, no. 2, 157–165.
- [2] Rudnicki, J.W. and J.R. Rice. 1975. "Conditions for the localization of deformation in pressure-sensitive dilatant materials." Journal of the Mechanics and Physics of Solids, 23, 371-394
- [3] Bažant, Z.P., and Pijaudier-Cabot, G. 1988, 'Nonlocal continuum damage, localization instability and convergence', Journal of Applied Mechanics. Volume 55 287-293
- [4] Shawki, T. G. 1994a. "An energy criterion for the onset of shear localization in thermal viscoplastic materials: Part I. Necessary and sufficient initiation conditions." Journal of Applied Mechanics, 61, 530-537
- [5] Shawki, T. G. 1994b. "An energy criterion for the onset of shear localization in thermal viscoplastic materials: Part II.

- Applications and Implications.” *Journal of Applied Mechanics*, 61, 538-547
- [6] Peerlings, R.H.J., R. de Borst, W.A.M. Brekelmans, and J.H.P. de Vree. 1996. “Gradient enhanced damage of quasi-brittle materials.” *Int. J. Numer. Meth. Engng*, 39, 3391-3403
- [7] Acharya, A., H.P. Cherukuri, and R.M. Govindarajan. 1999. “A new proposal in gradient plasticity: theory and application in 1-D quasi-statics and dynamics.” *Mechanics of cohesive-frictional materials*, 4, 153-170
- [8] Horstemeyer, M.F., Gokhale, A.M. 1999, “A void–crack nucleation model for ductile metals.” *International Journal of Solids and Structures*, vol 36, 33, 5029-5055
- [9] Fung, Y., Tong, P. 2001, “Classical and computational solid mechanics.” *World Scientific Publishing Co. Pvt. Ltd*, 483
- [10] Bazant, Z. P., and Zi, G. 2003. “Microplane constitutive model for porous isotropic rocks.” *Int. J. Numer. Anal. Meth. Geomech.* 27, 25-47
- [11] Regenauer-Lieb, K., and Yuen, D. A. 2003. “Modeling shear zones in geologic and planetary sciences: solid- and fluid-thermal-mechanical approaches.” *Earth-Science reviews*, 63, 295-349
- [12] Bazant, Z. P. 2004. “Scaling theory for quasibrittle structural

- failure.” Proc. of the National Academy of Science, 101(37), 13400-13407
- [13] Bazant, Z. P., and Di Luzio, G. 2004. “Nonlocal microplane models with strain-softening yield limits.” International Journal of Solids and Structures, 41, 7209-7240
- [14] Carol, I., Jirasek, M., and Bazant, Z. P. 2004. “A framework for microplane models at large strain, with application to hyperelasticity.” International Journal of Solids and Structures. 41, 511, 547
- [15] Hoek, E., C. Carranza-Torres and B. Corkum. 2004, “El criterio de Rotura de Hoek-Brown. Edición 2002” (Hoek-Brown Failure Criterion — 2002 Edition), in INGEOTÚNELES, Tunnelling Engineering Series, Vol. 7, Chapter 1, pp. 35-47. Madrid: Escuela Técnica Superior de Ingenieros de Minas, 2004
- [16] Salari, M.R. etal 2004, “A coupled elastoplastic damage model for geomaterials” Computer Methods in Applied Mechanics and Engineering, Volume 193, Issues 27-29, 2625-2643
- [17] Mainprice, D., Paterson, M. 2005, “Experimental deformation of flint in axial compression.” Materials science and engineering: Structural materials, Geological Society of London, Special edition 245, 251-276
- [18] Abd Al-Jalil, Y.Q. 2006. “The Mechanics of Indentation of

- Rock – A Critical Review”, The 41st Symposium of USRMS, Golden, Colorado, June 17-21
- [19] Abendroth, M. and Kuna, M. 2006. “Identification of ductile damage and fracture parameters from the small punch test using neural networks.” *Engineering Fracture Mechanics*, 73 (6), 710-725
- [20] Aydin, A., R.I. Borja, and P. Eichhubl. 2006. “Geological and mathematical framework for failure modes in granular rock.” *Journal of Structural Geology*, 83-98
- [21] Mediavilla, J., Peerlings, R. H. J., and Geers, M. G. D., 2006. “A nonlocal triaxiality dependent ductile damage model for finite strain plasticity.” *Comput. Methods Appl. Mech. Engrg.* 195, 4617-4634
- [22] Xue, L. 2007. “Damage accumulation and fracture initiation in uncracked ductile solids subject to triaxial loading.” *International Journal of Solids and Structures*, 44 (16), 5163-5181
- [23] Acharya, A. 2009. “Use of Thermodynamic Formalism in Generalized Continuum Theories and a Model for Damage Evolution.” *J. Engrg. Mech.* Volume 135, Issue 3, pp. 171-177